Ocean Modelling 184 (2023) 102231

Contents lists available at ScienceDirect

Ocean Modelling

journal homepage: www.elsevier.com/locate/ocemod

Efficient modeling of wave generation and propagation in a semi-enclosed estuary

Sean C. Crosby [a,b,*], Cornelis M. Nederhoff [a,c], Nathan VanArendonk [a], Eric E. Grossman [a,b]

[a] U.S. Geological Survey, 2885 Mission St., Santa Cruz, 95060, CA, USA
[b] Western Washington University, 516 High St., Bellingham, 98225, WA, USA
[c] Deltares USA, 8601 Georgia Ave, Silver Spring, 20910, MD, USA

ARTICLE INFO

Keywords:
Ocean waves
Prediction
Validation
Reduced-computation

ABSTRACT

Accurate, and high-resolution wave statistics are critical for regional hazard mapping and planning. However, long-term simulations at high spatial resolution are often computationally prohibitive. Here, multiple rapid frameworks including fetch-limited, look-up-table (LUT), and linear propagation are combined and tested in a large estuary exposed to both remotely (swell) and locally generated waves. Predictions are compared with observations and a traditional SWAN implementation coupled to a regional hydrodynamic model. Fetch-limited and LUT approaches both perform well where local winds dominate with errors about 10%–20% larger than traditional SWAN predictions. Combinations of these rapid approaches with linear propagation methods where remotely generated energy is present also perform well with errors 0%–20% larger than traditional SWAN predictions. Model–model comparisons exhibit lower variance than comparisons to observations suggesting that, while model implementation impacts prediction skill, model boundary conditions (winds, offshore waves) may be a dominant source of error. Overall results suggest that with a relatively small loss in prediction accuracy, simulations computation cost can be significantly reduced (by 2–4 orders of magnitude) allowing for high resolution and long-term predictions to adequately define regional wave statistics.

1. Introduction

Accurate, long-term, and high-resolution wave predictions are needed to assess the flood risk at the coast where rising sea levels and changing coastal conditions may alter wave propagation, generation, and extreme conditions on the shoreline (Erikson et al., 2015; Sweet et al., 2022). Phase-averaged numerical models, *e.g.,* Simulating WAves Nearshore (SWAN, Booij et al., 1999), are the defacto approach to predicting wave generation and transformation at the coast. While rapidly implemented when boundary forcing is available, models like SWAN require large amount computation for high-resolution simulation over long time periods. To reduce the computational cost the standard SWAN implementation may be replaced by faster reduced physics model (*e.g.,* O'Reilly and Guza, 1993; Leijnse et al., 2021) or by utilizing a look-up-table (LUT) approach (*e.g.,* Hegermiller et al., 2017). By neglecting the physics of sources, sinks, and non-linear interactions, wave energy is rapidly transformation is rapidly computed (Longuet-Higgins, 1957; Dorrestein, 1960; Crosby et al., 2018). This reduced physics approach is skillful where neglected terms are small, such as locations like the U. S. West Coast where low-frequency energy dominates. Here, the Coastal Data Information Program (CDIP, https://cdip.ucsd.edu/) makes operational wave predictions from buoy observations and linearly propagating wave energy to the shore (O'Reilly and Guza, 1993; O'Reilly et al., 2016). Prior work has also shown that along the shelf of Oregon and Washington, wind-wave generation is small compared to remotely-generated swell (García-Medina et al., 2013), illustrating why these rapid transformation approaches are so successful.

In contrast, a look-up-table (LUT) is typically a suite of simulations for a variety of forcing combinations with the complete model physics. The computation reduction comes from discretizing the range of possible forcings. This finite set of simulations is computed once and then predictions are simply queried for a given forcing condition. For example, in a small enclosed basin where wind conditions are spatially homogeneous, wind speeds and directions can be binned into discrete values covering the expected range and used as the set of plausible forcings. Waves are modeled for finite combination of speeds and directions forming a look-up table from which to generate rapid predictions (Golshani, 2011; Elliott and Neill, 2015). Similar approaches have been applied to the transformation of offshore waves to the nearshore (Hegermiller et al., 2017), but difficulties arise when the range of forcing conditions cannot be characterized within a manageable dimension, and total number of required simulations. For example, if local wind conditions and offshore waves are relatively

* Corresponding author at: U.S. Geological Survey, 2885 Mission St., Santa Cruz, 95060, CA, USA.
E-mail address: sean.crosby@wwu.edu (S.C. Crosby).

https://doi.org/10.1016/j.ocemod.2023.102231
Received 27 September 2022; Received in revised form 24 May 2023; Accepted 26 May 2023
Available online 7 June 2023

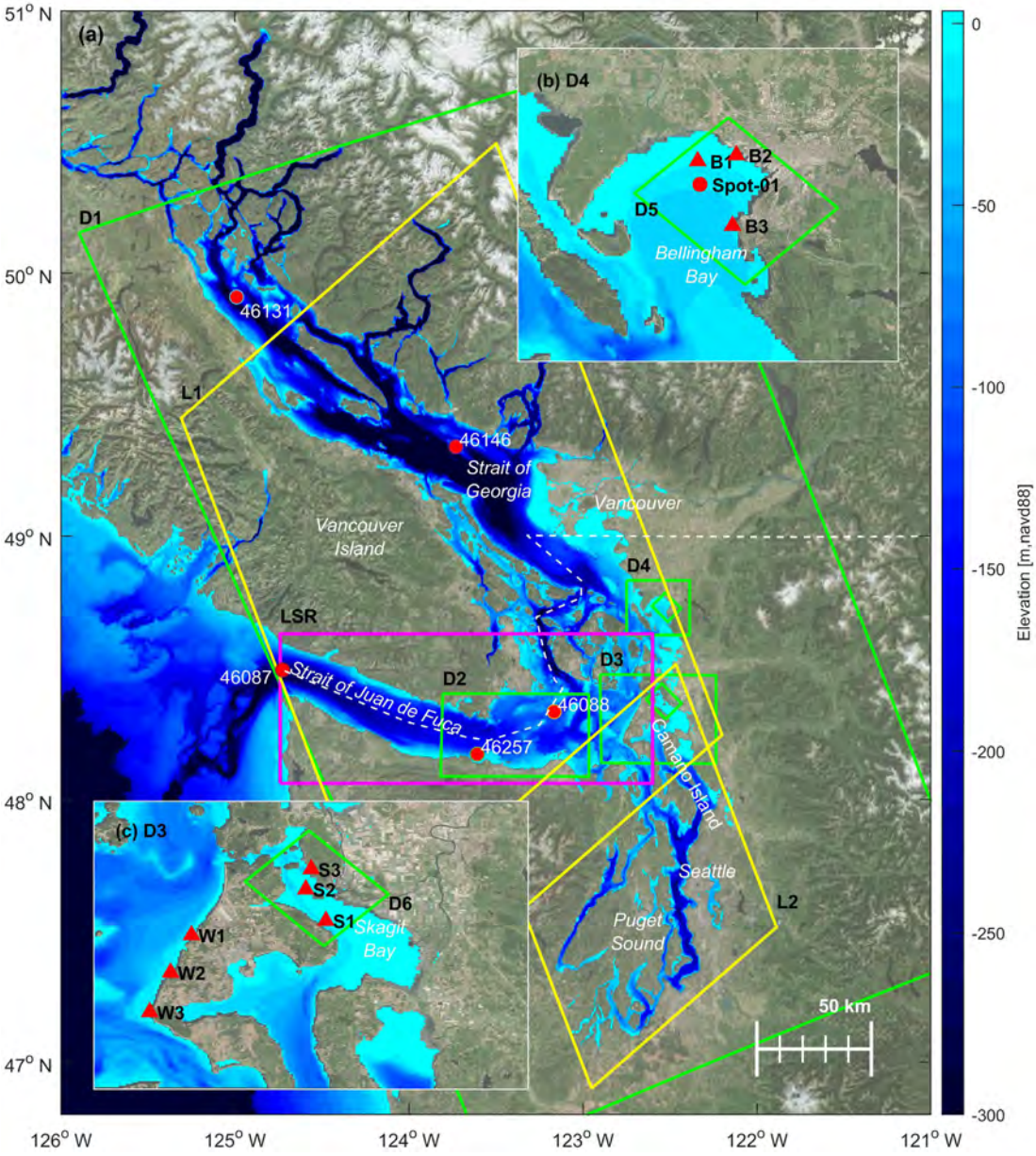

Fig. 1. Bathymetry, observation locations, and wave model domains (Table 2) in the Salish Sea. Domain grid extents are shown in green (SWM), magenta (LSR), and yellow (LUT) and labeled in black bold. Wave buoy locations are shown by filled red circles and bottom-mounted pressure sensors by red filled triangles (Table 1). Subsets (b) and (c) are zoomed to SWAN domains D4 and D3, respectively. Dashed white line shows international border between Canada and the United States.

uncorrelated the number of dissimilar forcing conditions, *i.e.,* offshore wave height, period, direction, wind speed, wind direction, becomes large. Additionally, offshore waves may not be well represented by a single set of bulk wave parameters (Kumar et al., 2017) or require additional spectral details (Crosby et al., 2016). Increasingly sophisticated statistical-modeling approaches have been developed to classify weather patterns, and using clustering and dissimilarity algorithms to generate a suite of possible model forcing (Camus et al., 2011, 2013); however, such approaches may fail with novel forcing conditions.

Reduced physics and LUT approaches both provide a trade-off between accuracy and the required computation and may be more appropriate in specific regions or frequencies. Here, we quantify the trade-off between accuracy and computational cost for several model implementations in a semi-enclosed estuary where both remotely and locally generated waves are significant. Section 2 introduces the region and prior wave studies are reviewed. Observations sites and data are reviewed in Section 3.1 and the varying modeling approaches are described in Section 3. Model skill and comparison throughout the region are assessed in Section 4, including the impacts of currents on waves in the region. Lastly, conclusions and results are summarized in Section 5

2. Regional background

The Salish Sea is a semi-protected estuary on the Washington and British Columbia coast. Glacially carved, it is a system of narrow straits, islands, sills, and basins all at varying spatial scales (Fig. 1). Exposed partially to the NE Pacific Ocean, both locally- and remotely generated waves are observed, with their relative impact depending on exposure. Strong currents (up to 5 m/s) in narrow tidal channels occur due to a large tidal range (3–4 m) and tidal prism (Thompson and Thomson, 1994).

Waves in the Salish Sea contribute to flooding at high water levels; erode unconsolidated shorelines, bluffs, and marshes; drive nearshore

Table 1
Locations and occupations of wave observations including short-term U. S. Geological Survey (USGS) bottom-mounted pressure sensor deployments and long-term National Data Buoy Center (NDBC) and Environment Canada (EC) directional wave buoy stations.

ID	Name	Lat [°]	Lon [°]	Depth [m]	Occupation
NDBC buoys					
46087	Neah Bay	48.493	−124.726	260	2004-Present
46088	Hein Bank	48.334	−123.165	114	2004-Present
46257	Angeles Point	48.173	−123.607	114	2020-Present
Environment Canada buoys					
46146	Halibut Bank	49.240	−123.730	42	1992-Present
46131	Sentry Shoal	49.910	−124.990	14	1992-Present
U. S. Geological Survey					
Spot-01	Bellingham Bay	48.742	−122.549	20	2/9/2020–1/2/2021
W1	Joseph Whidbey	48.318	−122.712	3	4/22/2019–9/4/2019
W2	Hastie Lake	48.274	−122.742	2	4/22/2019–9/4/2019
W3	Fort Ebey	48.227	−122.772	2	4/22/2019–9/4/2019
B1	Nooksack Delta	48.757	−122.551	4	12/11/2017–1/24/2018
B2	Squalicum	48.761	−122.519	3	12/11/2017–1/24/2018
B3	Post Point	48.715	−122.520	4	12/11/2017–1/24/2018
S1	Skagit Delta	48.335	−122.522	4	12/11/2017–2/9/2018
S2	Martha's	48.372	−122.551	3	12/11/2017–2/9/2018
S3	SneeOosh	48.396	−122.543	4	12/11/2017–2/9/2018

transport of sediments and pollutants important to shellfish, forage fish, and salmon habitats; and affect recreational and commercial boating activities that provide critical access to the many islands in the Puget Sound. Accurate, high-resolution, long-term wave predictions are thus critical to support shoreline planning, ecosystem restoration, and regional navigation and transportation (Finlayson, 2006b; Yang et al., 2019; Battalio et al., 2005; Gerstel et al., 1997)

Prior wave modeling studies, despite the region's complexities, show good predictive skill. Early predictions at Cama beach, located on Camano Island (Fig. 1), showed wave conditions are well modeled under stationary assumptions, likely because in the enclosed region with relatively short fetches local wind-wave generation reaches saturation rapidly (Finlayson, 2006a). A more recent regional wave study shows good skill at three moored buoy locations in the Strait of Juan de Fuca (SJF) and Strait of Georgia (SoG) with an unstructured grid and non-stationary model physics (Yang et al., 2019). The authors note the need to downscale wind predictions from 32 to 12 km to capture wind speeds in the region and derive a regional climatology based on a computationally costly, 5-year model simulation.

Though initial studies show predictive skill, comparison were made at the few wave observation sites and uncertainties remain regarding the impact of water levels and currents. Early observations suggest strong modulation of wave heights by tidal currents in the SJF, (Lambrakos, 1981), but model studies are still lacking. Recent work has shown significant impacts to waves by currents globally (Ardhuin et al., 2017; Gallet and Young, 2014) and in the Gulf Stream (Hegermiller et al., 2019); given the magnitude of currents in the region significant wave impacts are probable. To date, model validation of nearshore waves and their transformation and impacts across the shoreface are limited to the Cama Beach study (Finlayson, 2006a), despite recent flood impacts associated with waves. Rapid, accurate, and high-resolution approaches are needed to support ongoing flood hazard risk assessment.

3. Methods

Several wave modeling approaches were implemented, ranging in complexity from simple parameterized fetch- and depth-limited predictions, to numerical coupled hydrodynamic and wave simulations and are detailed below. In most cases waves were simulated from March 2016–December 2020 where high resolution meteorological forcing (Section 3.2.1) and observations (Section 3.1) are available.

3.1. Observations

Historic wave observations in the Salish Sea are sparse. The National Data Buoy Center (NDBC) currently maintains directional 3-m discus buoys located at the estuary entrance (46087) and inside the SJF (46257, 46088). Environment Canada additionally maintains two directional buoys in the SoG (46146 and 46131), see Fig. 1. To provide additional validation observations, including those close to shore, shallow bottom-mounted pressure gauges were deployed in Bellingham Bay (Fig. 1b), Skagit Bay, and on the west shore of Whidbey Island (Fig. 1c) for several months (Crosby and Grossman, 2019). Sites spanned a range of environments, from large to small basins, and with varying exposure to locally and remotely generated waves (Fig. 1). Wave conditions from pressure sensor observations were estimated following Jones and Monismith (2007).

3.2. Model inputs -test

3.2.1. Meteorological forcing

Winds and pressure fields were extracted from archived weather forecasts by Environment Canada (https://weather.gc.ca/), the highest resolution weather products freely available in the region. This High Resolution Deterministic Prediction System (HRDPS) is available at 1-h temporal and at 2.5 km spatial resolution with forty-eight hour forecasts every 6-h. Surface winds (10-m) are from the HRPDS-West domain were extract from forecast hours 1–6 and concatenated together to create a continuous time series of wind forcing. The zero forecast hour, or analysis, was found to be inconsistent with observations and therefore not used. Archived forecasts from March 2016 through 2020 provide nearly 5-years of forcing.

3.2.2. Bathymetry

Model depths were derived from high resolution bathymetry available in the region including 1-m digital elevation models (DEMs) by the U. S. Geological Survey (Tyler et al., 2020, 2021), 10-m coastal DEM by the National Ocean and Atmospheric Administration (NOAA, SJF & Port Townsend, Washington 1/3-arc second datasets, https://www.ncei.noaa.gov/), 3-arc second bathymetry dataset of British Columbia (https://www.ncei.noaa.gov/) and GEBCO 15-arc second global ocean and terrain model (https://www.gebco.net/data_and_products/gridded_bathymetry_data/). Bathymetry sources were merged with priority given to higher resolution and more recent sources, and then spatially averaged at model resolution before interpolation to model grids.

3.2.3. Offshore waves

The frequency-directional wave spectrum at the wave model offshore boundary is estimated from directional wave buoy observations at 46087 (Fig. 1). The NDBC buoy is located at the entrance to the SJF. Although directional spread estimates by the NDBC 3-m discus observations have been found to contain bias (approximately 6-deg), mean direction observations are skillful (O'Reilly et al., 1996), and energy propagation into the SJF is likely modulated at 1st order by offshore wave direction. The distribution of wave energy across offshore directions are estimated with observed directional moments ($a1$, $b1$, $a2$, $b2$, Longuet-Higgins et al., 1963) and the maximum entropy method (MEM, Lygre and Krogstad, 1986). While the directional distribution estimated from directional wave bouy observations is inherently uncertain Ochoa and Delgado-González (1990), model predictions driven by the MEM have previously been observed to be skillful (O'Reilly et al., 2016; Crosby et al., 2016).

3.3. Models

3.3.1. Hydrodynamic model

A depth-averaged hydrodynamic model was developed for the Salish Sea by Tehranirad et al. (2023) and summarized here. The Delft3D Flexible Mesh hydrodynamic model (Delft3D FM, Kernkamp et al., 2011) was developed with a spatial resolution varying from 150 to 1000-m. Surface and pressure forcing was derived from HRPDS forecasts. Offshore water levels were prescribed with tidal harmonics (Lyard et al., 2017, , FES2014b) and non-tidal water levels derived from HYbrid Coordinate Ocean Model (HYCOM, https://www.hycom.org/). Because HYCOM predictions do not include the inverse-barometer-effect, a reference pressure of 1017 mb is used in the model to capture changing water levels owing to atmospheric pressure adjustments. Fluvial forcing is prescribed for 23 major rivers in the region with USGS gauge data (Survey, 2016) and Canadian observations of the Fraser River at Hope, British Columbia (station 08MF005) (Canada, 2019). Modeled water level predictions have average errors of 15 cm.

3.3.2. Linear-shoaling-refraction (LSR)

Shoaling and refraction processes dominate wave propagation when wind-wave generation and non-linear processes are small (O'Reilly and Guza, 1993). This is often the case on the U.S. West coast when long-period remotely generated wave energy propagates in deep water over the relatively short continental shelf. Several prior studies have shown that good predictive skill is achieved with simple shoaling and refraction transformation of wave energy (O'Reilly and Guza, 1991, 1993; Crosby et al., 2016), and these techniques are currently used operationally by the CDIP to make accurate nearshore wave predictions (O'Reilly et al., 2016).

By ignoring wind-wave generation and non-linear interactions, nearshore and offshore wave energy can be related through a simple linear transformation. Historically this transformation was estimated by backward ray-tracing (Longuet-Higgins, 1957; Dorrestein, 1960; Mehaute et al., 1982). More recently transformations derived from phase-averaged wave modeling were shown to be similar when spatial resolution was sufficient (Crosby et al., 2018). Here, the phase averaged wave model, Simulating WAves Nearshore (SWAN, Booij et al., 1999), is used to relate offshore and nearshore wave energy in the SJF (Fig. 1) by simulating incoming wave energy from the range of possible directions.

The SWAN model domain covers the portion of the Salish Sea exposed to remote wave energy propagation through the SJF (Fig. 1, blue box). The model is run with varying incident wave direction, from 180 to 360-degrees at a 2-deg increments, covering the range of possible incident directions (*e.g.,* Fig. 2). Incoming wave energy, equivalent to 1-m in wave height, is prescribed at the boundary in a narrow 2-degree direction bin uniformly distributed across frequency for each simulation, similar to the approach in Crosby et al. (2018).

Table 2
Model domain (Fig. 1), the domain which it is nested, and its spatial resolution.

Model	Domain	Nest In	Resolution [m]
LSR	LSR	–	100
LUT	L1	–	100
	L2	L1	50
NWM/SWM	D1	–	1000
	D2	D1	200
	D3	D1	200
	D4	D1	200
	D5	D4	50
	D6	D3	50

The model is run in stationary mode (ignoring estimated propagation time-lags of 3–4 h) with 180 direction bins (2-deg resolution) and 48 frequency bins spaced logarithmically from 0.04 Hz to 0.5 Hz and at a spatial resolution of 100-m (Table 2). Simulations were run with constant water level equal to mean-sea-level (MSL) and currents were ignored. Second order numerics (SORDUP) produced significant garden sprinkler effect (see SWAN technical manual) and therefore first order (BSBT) propagation numerics were used. Wind-wave generation, white-capping, and diffraction are all disabled while bottom friction and breaking constants are set to default values. Convergence criteria was met for all simulations, requiring that in over 99% of cells the change in wave heights change were less than 2% or 2 cm between the last and prior iteration. Computation of all model simulations on a 12-core desktop (AMD Ryzen 3.8 GHz) at 100-m resolution took less than 1-day. Throughout this study SWAN version 41.10 or later (41.20 and 41.31) were used.

Frequency-directional energy spectra are saved at observation sites and at model grid cells (Fig. 1). Following Crosby et al. (2018), transform coefficients, K, are estimated from the ratio of nearshore, E_n, and offshore energy, E_o such that at location i,

$$K[i,f,\theta_o,g(\theta_n)] = \frac{\int E_n(i,f,\theta_n) g(\theta_n)\, d\theta_n}{E_o(f,\theta_o)},$$
$$\text{where} \quad g(\theta_n) = (1, \cos\theta_n, \sin\theta_n, \cos 2\theta_n, \sin 2\theta_n). \tag{1}$$

The function $g(\theta_n)$ allows for an estimate of total wave energy and directional buoy moments $a1$, $b1$, $a2$, $b2$, respectively (Longuet-Higgins et al., 1963). Offshore frequency-directional spectra at the model boundary, E_b, are estimated from observations at 46087 (Section 3.2.3). A simple integration of the offshore spectra and transform coefficients provides predictions of wave energy, E, at a time step, t, where

$$E(t,f) = \int K(f,\theta_o,1)\, E_b(t,f,\theta_o)\, d\theta_o, \tag{2}$$

and predictions of directional moments, *e.g.,* a_1, are similarly estimated,

$$a_1(t,f) = \int K(f,\theta_o,\cos\theta_n)\, E_b(t,f,\theta_o)\, d\theta_o. \tag{3}$$

Predictions are made within the model domain (LSR, Table 3) for the period of available HRDPS meteorological forecasts (Section 3.2.1).

3.3.3. Fetch-depth-limited (FDL)

While LSR models wave propagation, other methods are needed for wind-wave generation. Over decades empirical relations between wind, waves, fetch, and water depth been developed and is best described by the non-dimensional variables: non-dimensional energy, $\epsilon = g^2 E/u^4$, non-dimensional frequency, $\nu = f_p u/g$, non-dimensional fetch, $\chi = gx/u^2$, and non-dimensional depth, $\delta = gd/u^2$. Here, g is the gravitational constant, E is the wave energy variance in m^2, u is the wind speed, f_p is the peak wave period, and x is fetch. The comprehensive JONSWAP experiment in the North Sea (Hasselmann et al., 1973) was the first to use multiple observations sites with varying fetches and derived empirical relationships for ϵ and ν are found in CERC (1984).

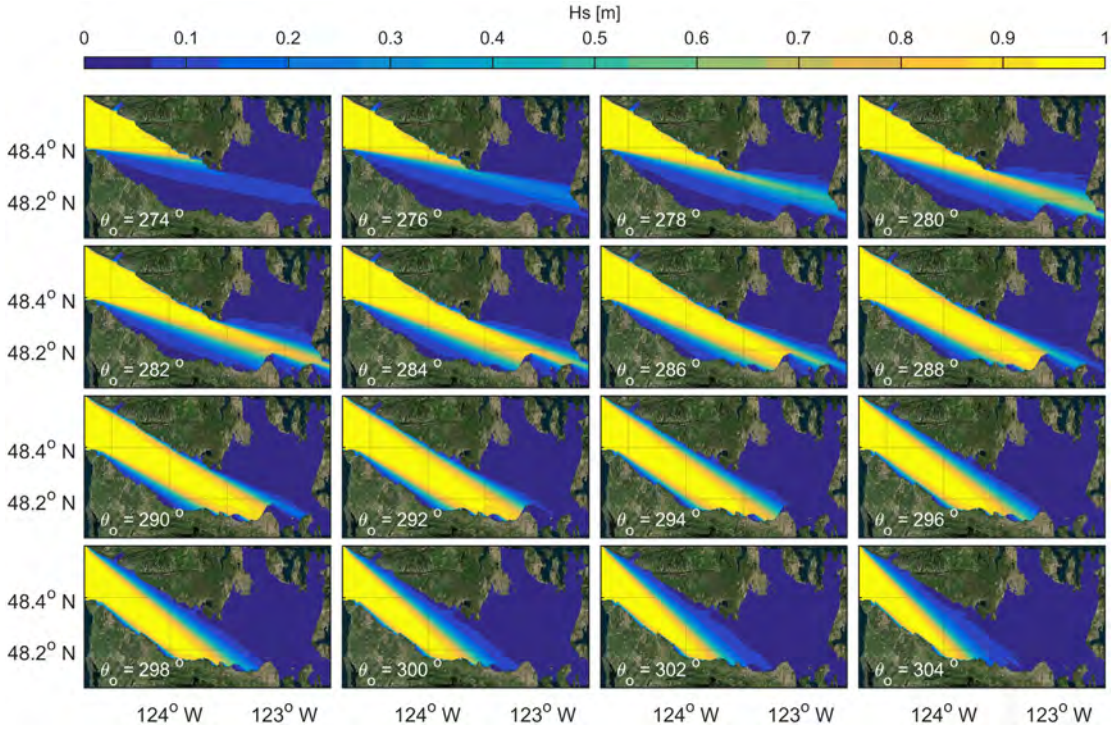

Fig. 2. Linear Spectral Refraction (LSR) model runs for a selection of incoming wave directions (θ_o, black text). Wave heights are shown in color. Note that simulations are computed from 180 ° -360 ° at 2 ° increments and incoming wave energy is evenly distributed across frequency bands (0.04 – 0.5 Hz).

Lacking similar data is shallow water, Young and Verhagen (1996) examined an array of shallow wave observations in Lake George, Australia. An array of observations sites in the shallow lake (nearly constant 2-m depth) provided additional constraints and relationships for ϵ and ν where

$$\epsilon = 3.64 \cdot 10^{-3} \left[\tanh A_1 \tanh\left(\frac{B_1}{\tanh A_1}\right)\right]^{1.74},$$
$$\nu = 0.133 \left[\tanh A_2 \tanh\left(\frac{B_2}{\tanh A_2}\right)\right]^{-0.37}, \quad (4)$$

and

$$A_1 = 0.493\,\delta^{0.75},$$
$$B_1 = 3.13 \cdot 10^{-3} \chi^{0.57},$$
$$A_2 = 0.331\,\delta^{1.01}, \quad (5)$$
$$B_2 = 5.215 \cdot 10^{-4} \chi^{0.73}.$$

These relations are used to estimate significant wave height, H_s, and peak period, T_p where

$$H_s = 4\sqrt{u^4 \epsilon / g^2}, \qquad T_p = \frac{u}{\nu g}. \quad (6)$$

Fetch, x, is estimated by tracing rays from a given location until they reach land, defined as a water depth less than 1-m (*e.g.,* 3). Rays are traced in spherical coordinates by integrating the geodesic equations at 100-m steps (Munk et al., 1988) where a 100-m step size was found to be sufficient to avoid missing small islands and narrow spits. Rays are traced from the prediction site at a starting angle, θ, from 0–360 degrees with 1-deg increments. Tracing yields a function $x(\theta)$ (*e.g.,* Fig. 3a). For a given wind direction, θ_w, the effective fetch, $\hat{x}$ is

$$\hat{x} = \frac{\int x^{\alpha}(\theta) W(\theta,\beta)\, d\theta}{\int x^{\alpha-1}(\theta) W(\theta,\beta)\, d\theta} \quad (7)$$

where

$$W(\theta,\beta) = \begin{cases} \cos^{2\beta}(\theta - \theta_w) & \text{where } -\pi/2 \geq \theta \leq \pi/2 \\ 0 & \text{otherwise} \end{cases} \quad (8)$$

Here, $W(\theta,\beta)$ is a weighting function with width determined by β. Scaling parameter α determines the emphasis of peaks in $F(\theta)$, where a large alpha weights peaks more heavily than valleys. Small values of β result in a wide weighting function that considers a larger range of fetch values surrounding a given wind direction (*e.g.,* A1). The largest $\hat{x}$ are therefore derived from large α and small β values by allowing for a broad weighting function and weight peaks heavily (Fig. 3b). The weighting in (7) results in a smoother change in fetch with direction and tends to ignore small islands that wave energy is likely to refract or diffract around (O'Reilly and Guza, 1993). Additionally, α and β allow for tuning based on observations. Optimal values of $\beta = 1$ and $\alpha = 1$ were selected based on overall agreement with observations (see, Appendix A.2)

Wind direction, θ_w, and speed, u, from HRDPS forecasts are extracted at the prediction location. The argument may be made for extracting wind speed from some upwind direction, but for simplicity only wind conditions at the prediction location are used. Water depths at each modeled time-step, d, are derived from numerical hydrodynamic simulations described in Section 3.3.1.

3.3.4. Look-up-table (LUT)

An alternative to the simple and computationally fast FDL approach, is the incrementally more sophisticated and computationally taxing method of creating a look-up-table (LUT) of pre-computed wave simulations. A LUT is an approach to reducing computation when forcing conditions can be parameterized into a small number of variables, and those forcing combinations can be pre-computed over the range of expected values. When the number of combinations is less than the time-steps of the simulation computation costs are reduced.

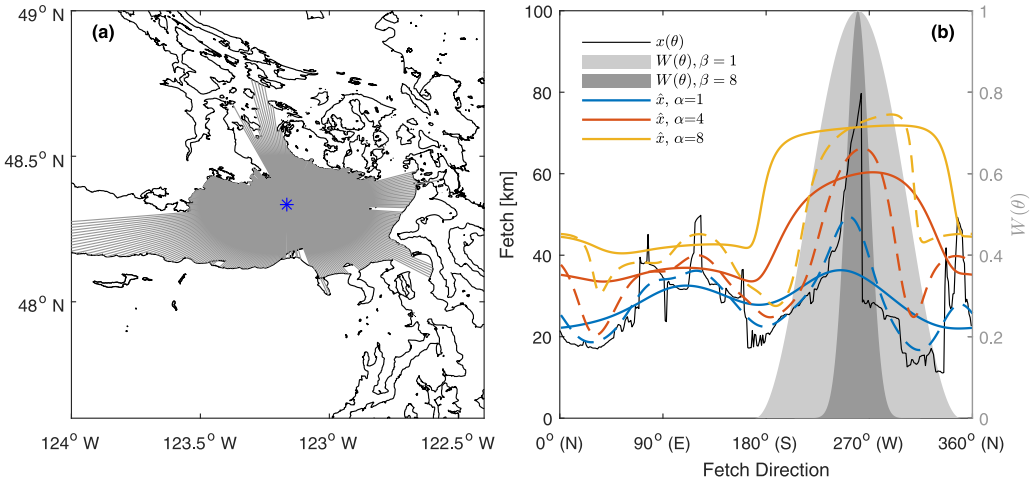

Fig. 3. (a) Rays (gray) traced from Hein bank (blue asterisk) at 1° direction intervals terminating at land determine fetch extent. (b) Fetch (solid black) versus fetch direction. Effective fetch, $\hat{x}$, is shown with varying α (colors, see legend) and for $\beta = 1$ (solid lines) and $\beta = 16$ (dashed lines). The weighting function, $W(\theta)$, is illustrated in light gray for $\beta = 2$ and dark gray for $\beta = 16$ shading with scaling on the right-hand y-axis.

Table 3
Model description and prescription of model forcing with a yes/no (Y/N) flag indicating if the model was forced by offshore waves (Offshore), regional winds (Wind), regional currents (Currents) and a flag to indicate whether stationary (S) or non-stationary (N) numerics were used in SWAN simulations. Simulated time periods are denoted with an X.

Model	Description	Offshore	Wind	Currents	Numerics	2016–2020	Oct-Nov 2019
FDL	fetch-depth-limited	N	Y	N	–	X	
LSR	linear-shoaling-refraction	Y	N	N	S	X	
LUT	SWAN look-up-table	N	Y	N	S	X	
SWM	stationary SWAN	Y	Y	N	S		X
SWM+C	stationary SWAN + current	Y	Y	Y	S	X	
NWM+C	non-stationary SWAN + current	Y	Y	Y	N		X

Prior wave studies have applied a LUT approach to transform waves nearshore (Hegermiller et al., 2017) and predict wind-wave generation in enclosed basins (Elliott and Neill, 2015; Golshani, 2011). For wind-wave generation, wind conditions are assumed homogeneous across the model domain and a range of wind speeds and directions are simulated.

Here, stationary SWAN simulations are computed for a suite of wind speeds, 0 to 30 m/s in 2.5 m/s increments, wind directions, 0 to 360 ° in 20 ° increments, and water levels, −2 to 8.5 m+navd88 in 1.5 m increments for a total of 1,728 model runs (*e.g.,* Fig. 4). Two model domains cover the region, L1 and L2, with directional resolution of 100 m and 50 m, respectively (Tables 2 and 3). Domain L2 is nested inside of domain L1 along the north-west boundary (Fig. 1). The models are run in stationary mode with 72 direction bins (5-deg resolution) and 45 frequency bins spaced logarithmically from 0.03 Hz to 2.0 Hz with default third generation wave growth and white-capping parameters. Diffraction is disabled and bottom friction and breaking constants are set to default values. Convergence criteria were set similarly to LSR simulations (Section 3.3.2). Computation is performed on the USGS computer cluster, Yeti (Anon, 2021), requiring 36-days of compute on a single 20-core node (Intel Ivy Bridge). Several nodes were used simultaneously allowing for computation to complete in several days.

Wave predictions are generated at given locations with local water level predictions (Section 3.3.1) and the nearest over-water wind predictions (Section 3.2.1). At each time-step the LUT of desired wave parameters (*e.g.,* H_s, T_p, T_m, D_m) is linearly interpolated (3-dimension) to the predicted water level, wind speed, and wind direction. Predicted energy spectra, $E(f)$, is similarly interpolated at observation locations where spectral predictions are saved. Predictions are created over the time period with available HRDPS forecasts (2016–2020).

3.3.5. LSR+FDL and LSR+LUT

Combining the LSR predictions with FDL or LUT predictions offers a computationally rapid approach to capturing both offshore energy penetration and regional wind-wave generation. These calculations are done under the following assumptions: (1.) wind-wave generation is unaffected by existing sea state; (2.) nonlinear wave–wave interactions between locally generated and remotely generated waves are insignificant; and (3.) that all simplifying assumptions in LSR and LUT are additionally valid. Under these assumptions wave energy spectra from remote- and local-generation is simply additive. In practice, file storage limitations do not allow for saving frequency-directional spectra at all time steps and model locations. However, where only bulk parameter predictions are saved wave heights can be added in quadrature (*e.g.,* $H_s^{(3)^2} = H_s^{(1)^2} + H_s^{(2)^2}$), and mean frequency, f_m, is determined by a weighted average,

$$f_m^{(3)} = \frac{H_s^{(1)^2} f_m^{(1)} + H_s^{(2)^2} f_m^{(2)}}{H_s^{(1)^2} + H_s^{(2)^2}}. \tag{9}$$

Mean wave directions can be similarly estimated by a weighted average, but with care taken to use a circular mean; however this was not done here.

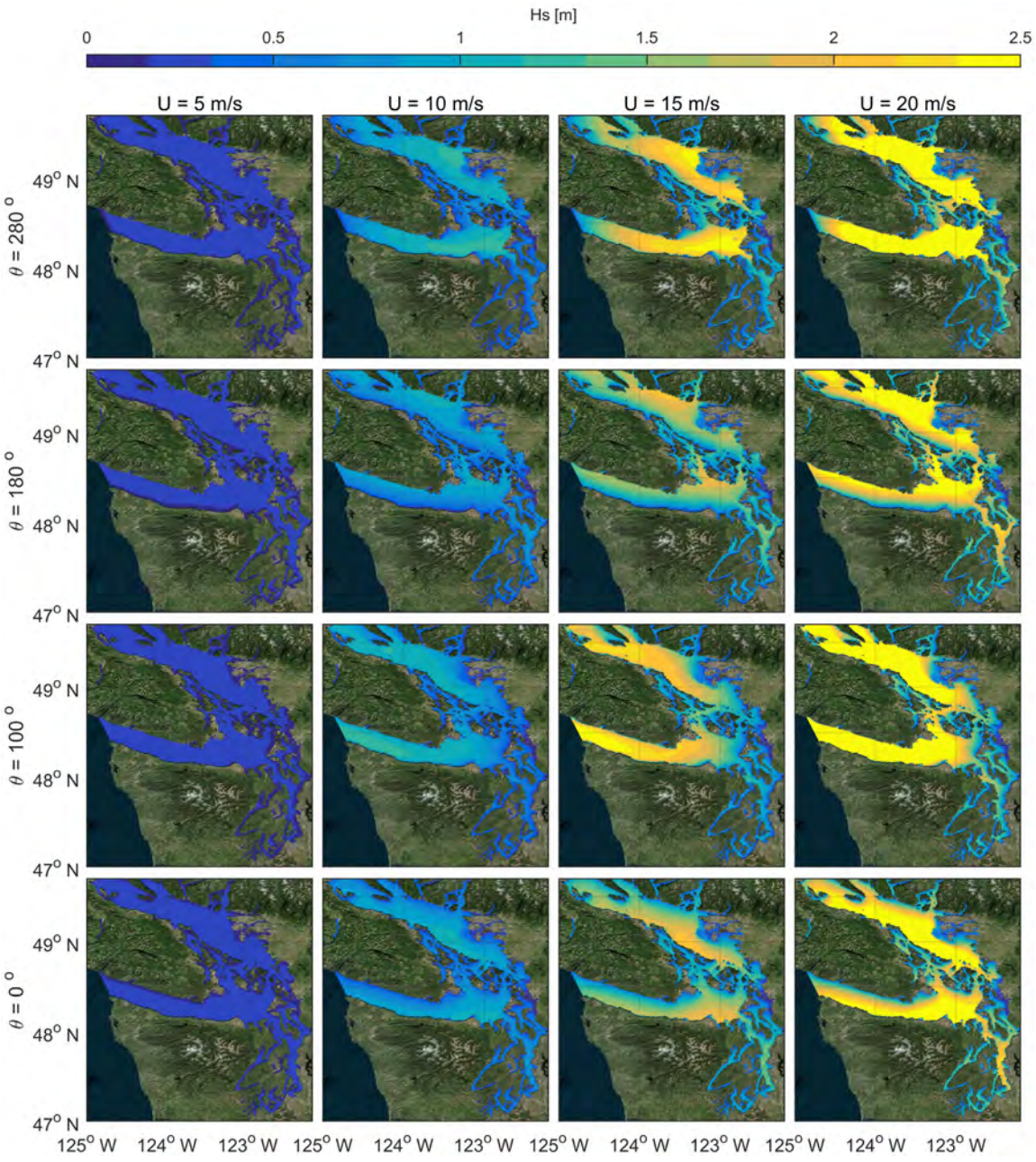

Fig. 4. Wave heights for several Look-up-table (LUT) model runs for varying wind speeds (columns) and wind directions (rows).

3.3.6. Stationary and non-stationary wave model (SWN,SWM+C, NWM)

A more robust, but computationally demanding approach to wave prediction, is implementation of a phase averaged wave model for continuous simulation. Here, SWAN was coupled to the regional hydrodynamic model of water level and currents (Section 3.3.1) with the Delft3D Flexible Mesh Modeling Suite developed by Deltares. SWAN was configured in both stationary and non-stationary modes as well as with and without coupling to depth-averaged currents. Spatially varying winds from HRDPS (Section 3.2.1) provide input to local wind-wave generation and waves observed at 46087 (Section 3.2.3) provide offshore (spectral) forcing.

To allow for feasible computation a large overall SWAN domain was created at 1 km spatial resolution with several nested, and sub-nested domains (Table 2, Fig. 1) at resolutions increasing with a factor 5 to 200-m (nested) and 50-m (sub-nested). Nested domains are created at locations with available observations and much of the larger region was not resolved beyond the relatively coarse 1-km.

To evaluate differences and model skill three configurations were simulated, stationary numerics without wave–current interactions (SWM), stationary numerics with wave–current interactions (SWM+C), and non-stationary numerics with wave–current interactions (NWM +C). A time step of 10-min was used in non-stationary simulations, while outputs and stationary simulations were computed at hourly intervals. The models are similar to LUT simulations (Section 3.3.4, however the number of direction bins was reduced to 36 (10-deg resolution) to lower computational expense. Convergence criteria were set similarly to LSR simulations (Section 3.3.2) but with a maximum number of iteration of 50 in the stationary simulations. It was found

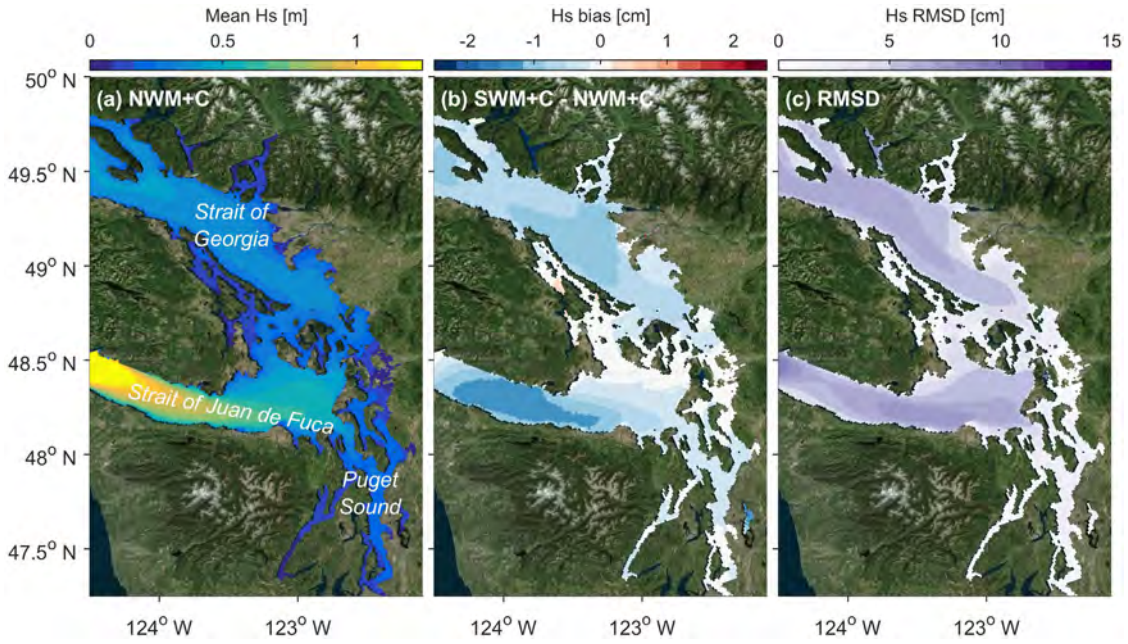

Fig. 5. (a) Non-stationary (NWM+C) mean modeled wave heights from Oct 1 2020 through Nov 30 2020. Mean wave height bias, (b), and root-mean-squared-difference, (c), between stationary (SWM+C) and non-stationary simulations (SWM+C - NWM+C).

to be necessary in non-stationary simulations to increase the maximum number of iterations from the default of 1 to 10.

3.4. Simulation time periods

Wave simulations were performed over two time periods (Table 3). Owing to computational constraints, SWM, SWM+C, and NWN+C simulations were completed during the comparatively short 2-month period from October to November of 2019. Longer 5-year simulation were computed for SWM+C and all rapid approaches (FDL, LSR, LUT) from 2016–2020 where both HRDPS wind forcing (Section 3.2.1) and regional wave observations were available (Table 1).

4. Results and discussion

Overall results suggest that including additional physics in numerical models tends to improve prediction skill, however, this improvement is in some cases marginal and may not be worth the computational expense. Below, predictions with stationary and non-stationary numerics are compared, the impact of wave current interactions are evaluated, and reduced-physics model implementations are compared.

4.1. Non-stationary vs stationary

Stationary and non-stationary simulations should begin to diverge where the domain is large enough such that the sea state does not fully develop within the model time step (1-h). Comparisons of SWM+C and NWM+C significant wave height (H_s) predictions from Oct-Nov 2019 show the largest root-mean-squared-differences (RMSD) of 5–10 cm in the regions with the largest basins, such as the SoG and SJF and smaller differences (0–5 cm) in smaller basins such as those within near Seattle (Fig. 5, Fig. 1). These differences appear to be primarily a result of timing as mean bias between SWM+C and NWM+C are comparatively small (0–2 cm). On average, SWM+C simulations produce slightly higher wave heights resulting in a consistent negative bias across the domain (Fig. 5b).

Table 4
Root-mean-square-error (RMSE) and bias at three observation sites (rows) for three model configurations (rows) for the simulation period Oct-Nov 2019 (Table 3).

Site	*Hs RMSE* [cm]			*Hs bias* [cm]		
	SWM	SWM+C	NWM+C	SWM	SWM+C	NWM+C
46257	30	31	29	6.0	6.6	7.6
46146	23	–	18	−3.0	–	−2.1
Spot-01	13	13	12	1.1	1.0	1.2

Prediction errors are also examined for both models. Root-mean-squared-error (RMSE) at three observation sites with data during this period are lower by 1–5 cm for NWM+C predictions compared to SWM+C predictions (Table 4). The largest improvement is observed at 46257 and 46146 both located in larger open basins (Fig. 1). Bias at observations sites is relatively similar for NWM+C and SWM+C, within 1–2 cm, and range from −3 to 8 cm (Table 4). Overall, the error with observations is larger than the differences between models suggesting the dominant error terms are not stationary/non-stationary assumptions. While accuracy is improved with non-stationary assumptions, the computational cost of non-stationary simulations were approximately 3x that of stationary simulations.

4.2. Current effects

Over the shorter simulation period (Oct-Nov 2019) stationary simulations (SWM) are compared with and without currents (Table 3). Mean normalized bias (Appendix A.1), SWM+C - SWM, varies from 10%–40% with the strongest negative values east and west of Dungeness Spit where depth averaged mean currents show a clockwise circulation pattern (Fig. 6a). Mean wave heights are generally 10%–20% higher for SWM+C predictions in the northern part of domain D2 (Fig. 6). Here, the region is sheltered from offshore energy in the SJF by the southern most tip of Vancouver Island. Current refraction is likely increasing the directional spread in wave conditions allowing for additional energy penetration into sheltered regions (Ardhuin et al., 2017). Differences between mean wave heights in domains D3 and D4 are much smaller

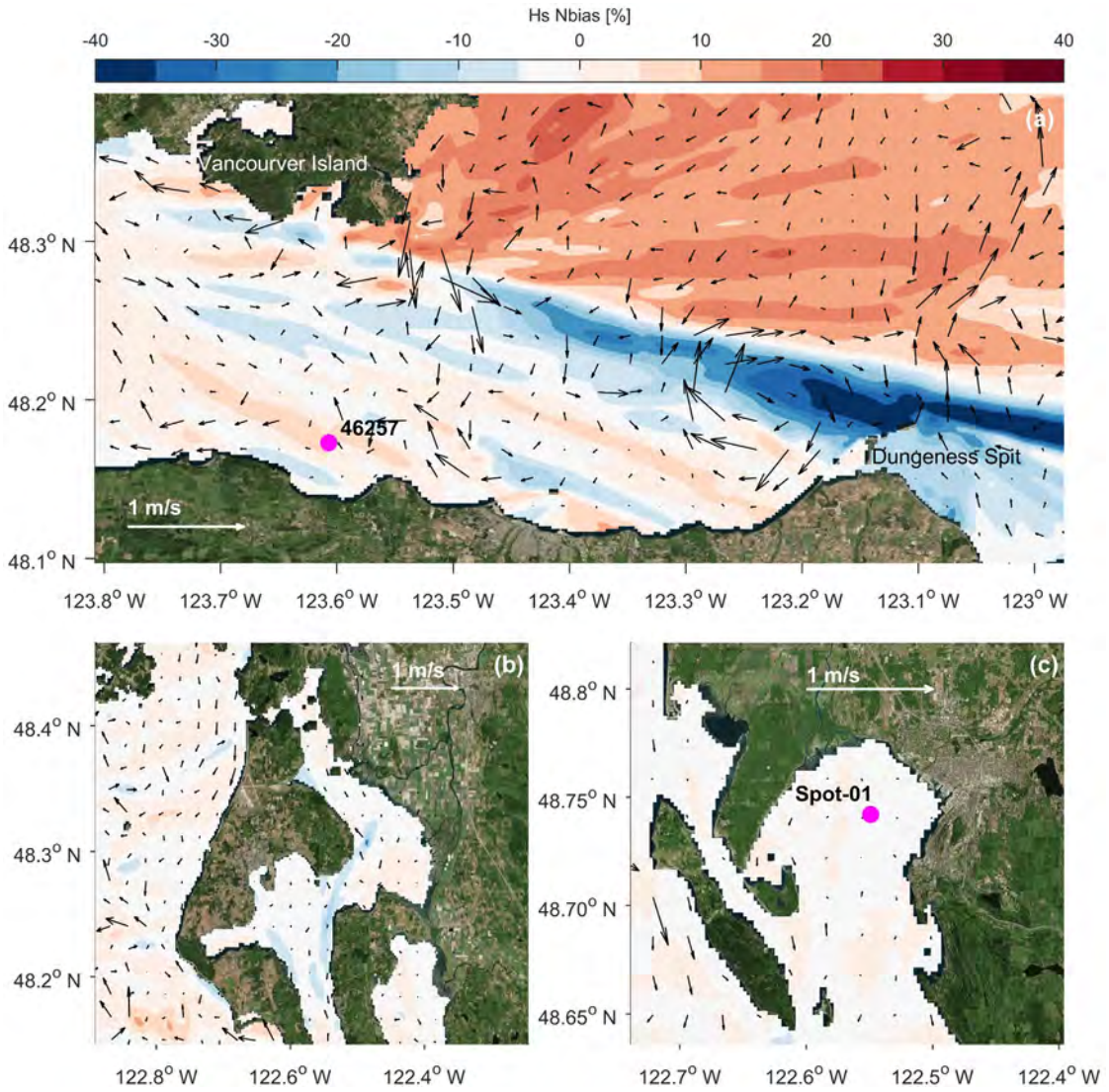

Fig. 6. Normalized wave height bias (Nbias, see appendix A.1) between stationary runs with currents (SWM+C) and without (SWM) predictions for domains (a) D2, (b) D3, and (c) D4 (Table 2) for predictions from October to November 2020. Black arrows show mean depth-averaged current velocity with white arrow and text providing scale. Magenta circles show locations wave buoys (Table 1).

as currents at these locations are slower (Fig. 6b,c). Similar patterns of Root-mean-squared-differences (RMSD) in wave heights are observed with differences ranging from 0%–50% in domain D2 and much less in domains D3 and D4 (Fig. 6).

Prediction errors for SWM and SWM+C at observation sites available during the simulation period are surprisingly similar (Table 4). While SWM+C errors are slightly larger at 46257 this difference is not likely significant. This prediction error similarity is likely because 46257 is at site of strong current shear (Fig. 7). Further study is needed to quantify both the accuracy of current predictions and the potential improvement in prediction accuracy possible by including currents in wave simulations.

4.3. Accuracy at observation locations

Overall predictions during the nearly 5-year simulation period (Table 3) were skilled, with increasingly complex and computationally costly models performing slightly better. Fourteen-day time series at observation locations illustrate some differences and deficiencies (Fig. 8). At locations partially sheltered to offshore wave energy (46088, W1, W2, W3) LSR under-predicted because of the lack of local wind-wave generation (Fig. 8a,i,m,n). At the relatively exposed location, 46257, LSR predictions showed better agreement with observations at most times, but local wind-waves appeared important as well, as indicated by FDL and LUT predictions (Fig. 8d).

Modeled wave heights at completely sheltered locations, *i.e.,* not exposed to remote wave energy, were most similar. Predictions in Bellingham and Skagit bays in general show good agreement with observations and between models (SWAN+C, LUT, and FDL) with the exception of locations S1 and S2 where all models were biased low (Fig. 8i,j). Under-predicted wind speeds are suspected as the primary drive of this bias, however, robust wind observations were not available at this location to confirm this hypothesis. In larger basins, such as the SoG and inside the SJF, peak wave heights appeared over-predicted by the LUT approach, but FDL and SWAN+C were similar and more closely aligned with observations (Fig. 8a,b,c).

Predictions at 46257 were examined more closely as the site is most exposed to remotely generated energy, while local generation still

Table 5
Median RMSE and bias across observations sites for several models (rows) as illustrated in Fig. 11. Median errors/differences are computed with respect to observations (left) and SWM+C predictions (right) and additionally for both all wave conditions ($Hs \geq 0$ m) and solely for relatively large waves ($Hs \geq 0.5$ m). Note that errors at B3 are not included as SWM+C predictions are not available there.

Threshold	Model	Error to observations				Difference to SWM+C			
		Hs [m]		*Tm* [s]		*Hs* [m]		*Tm* [s]	
		RMSE	bias	RMSE	bias	RMSD	bias	RMSD	bias
Hs ≥ 0 m									
	SWM+C	0.17	−0.02	1.2	−0.6	–	–	–	–
	FDL	0.22	−0.07	1.5	−0.9	0.14	0.00	0.7	0.1
	LSR	0.39	−0.27	5.8	5.5	0.33	−0.25	6.7	6.5
	LUT	0.19	−0.03	1.7	−1.1	0.12	0.00	0.8	0.1
	LSR + FDL	0.21	−0.05	1.4	−0.3	0.14	0.00	0.9	0.5
	LSR + LUT	0.17	−0.01	1.7	−0.7	0.12	0.00	0.8	0.1
Hs ≥ 0.5 m									
	SWM+C	0.31	−0.11	0.7	−0.1	–	–	–	–
	FDL	0.36	−0.27	0.7	−0.2	0.22	−0.11	0.7	0.1
	LSR	0.80	−0.74	5.7	5.5	0.68	−0.64	5.5	5.3
	LUT	0.31	−0.07	0.9	−0.2	0.18	0.04	0.8	0.3
	LSR + FDL	0.34	−0.22	0.8	0.4	0.21	−0.10	0.9	0.8
	LSR + LUT	0.29	−0.07	0.9	−0.2	0.18	0.04	0.7	0.3

relatively important. LSR+LUT and LSR+FDL wave height predictions showed good agreement with SWAN+C despite the simplifications employed (Fig. 9a). Overall SWM+C predictions appeared slightly higher during this time period, while LSR+LUT and LSR+FDL appeared more closely aligned with observations. Mean wave period was also well predicted by LSR+LUT and LSR+FDL and showed clearly the oscillation between remotely and locally generated wave conditions (Fig. 9b). Mean wave direction was also well predicted, though it is clear that NW energy both from local winds and offshore waves tend to dominate.

Across observation locations SWAN+C and LSR+LUT wave height predictions showed the best agreement with observations (Fig. 10). At most locations LSR+FDL predictions had a negative bias, indicated by quantile–quantile curves (magenta, Fig. 10). At some locations LSR+LUT wave height distributions appeared closest to observations, while at others SWM predictions appeared best. At S1 and S2 a clear negative bias was present for all model configurations, confirming that the observed biases in Fig. 8 were typical throughout the record.

Wave height root-mean-squared-error (RMSE) varied across locations but was lowest for SWM+C predictions at most sites (green bars in Fig. 11a). This was similarly true for mean wave periods (Fig. 11b). While LSR+LUT wave height errors were lower than LSR+FDL, mean wave period errors were higher. Larger LSR+LUT RMSE occurred most strongly at sites 46088, W1, W2, and W3, located just inside the SJF. This appears driven by larger negative bias in mean wave height prediction (Fig. 11d). Wave height biases varied, but are mostly consistent between models, suggesting that either models contain a very similar bias or that model forcing biases are driving these errors (Fig. 11c). For example, the largest biases were observed at W1–W3 where small amounts of offshore energy propagation may be difficult to resolve and highly influence by directional details not resolved well by the directional coefficients measured by 46087 (Ochoa and Delgado-González, 1990).

Median RMSE from all observations sites (except for B3 where SWM+C predictions are not available) for SWM+C and LSR+LUT were similar (17 cm, Table 5). Median RMSE was 21 cm for LSR+FDL and slightly higher for FDL alone (22 cm). Lowest errors for mean period were achieved by SWM+C followed by LSR+FDL. With the exception of LSR, median bias for wave height and mean period were small as positive bias in some regions tended to cancel out negative biases in others. Median wave height RMSE in LUT only predictions was relatively low because most observation sites were not exposed to remote energy. Overall prediction error was low for the combined models, LSR+FDL and LSR+LUT, and was similar to SWM+C accuracy when averaged across locations and conditions (17–21 cm wave height RMSE, Table 5). Errors and biases increase when limiting the error analysis to waves conditions where $Hs \geq 0.5$ m, but the comparison between models stays mainly the same. Surprisingly wave height errors and bias are slightly lower for LSR+LUT predictions compared to SWM+C, but SWM+C mean period predictions are still more skilled (Table 5).

Mean observed and predicted energy as a function of frequency illustrate where offshore energy and local wind generation tend to dominate observations and predictions (Fig. 12). At 46257, the site most exposed to offshore wave energy, 10-s energy was the largest contributor and was under-predicted by both SWM+C and LSR (Fig. 12a). The combined LSR+LUT mean energy predictions agree better with observations than SWM+C predictions that appeared biased high at higher frequency and biased slightly lower at lower frequency. While LSR+LUT appeared best at exposed site 46257, at the mostly sheltered 46088 location mean SWM+C predictions agreed better with observations (Fig. 12b). This is likely due to the LSR predictions underestimating remotely generated energy propagation and the neglected non-linear interactions between remotely and locally generated energy in LSR+LUT. In contrast, results at W1–W3 were more similar for SWM+C and LSR+LUT models (Fig. 12c–e). At sheltered sites the LUT and SWM+C spectral predictions were mostly similar and agree generally with observations. At 46146, mean SWM+C predictions were closer to observations while LUT predictions exceed observed values (Fig. 12f). In larger basin winds are much more likely to be spatially heterogeneous and LUT assumptions will more often be violated. In smaller embayments, such as Bellingham Bay, observations and models agree quite closely with the exception of B3, that is very close to shore and likely not well resolved by the model spatial resolution (Fig. 12h–k).

4.4. Model–model differences

In most cases, model–model differences are smaller than model errors with observations. Root-mean-squared-differences (RMSD) are estimated between SWM+C, and LSR+FDL and LSR+LUT models at observation locations and shown in red outlines in Fig. 11a,b. With the exception of S1–S3, wave height and mean period errors between these reduced-physics models (LSR+FDL, LSR+LUT) and SWM+C are lower than errors with the observations themselves. This suggests that either the models are prone to errors in very similar ways, or that uncertainty in the model forcing dominates prediction error (*e.g.,* biases in wind predictions, errors in bathymetry, or poorly resolved directional wave spectra offshore). Results are similar for model biases, but less consistent, and in some locations model–model bias and mode-observation is similar. Median RMSD and bias across observation sites are consistent with these findings indicating that model–model differences are generally lower than model errors to observations (Table 5).

While observation sites are sparsely dispersed across the domain, model–model comparisons illustrate differences spatially across the complex region. Owing to data constraints, spatial outputs were compared over the shorter 2-month time period during October and November of 2019. Mean wave heights during this time vary between models, but are similar for SWM+C and LSR+LUT predictions (Fig. 13a-d). Mean bias between simplified models and SWM+C shows clearly where offshore energy (LSR) and locally generated energy (LUT) dominate (Fig. 13e,f). In the SJF bias between LSR and SWM+C is relatively small, up to 0%–30% of the mean wave height while root-mean-squared-differences (RMSD) normalized by mean SWM+C wave heights (Fig. 13a) are 0%–50% (Fig. 13e,h). In the SoG and protected part of Puget Sound errors and bias between SWM+C and LUT are small, 10%–30%. The combined model, LSR+LUT, misfit to SWM+C is relatively small in most places, with bias and RMSDs just 10%–20% of the mean wave height. Some exceptions are observed in narrow bays and inlets where SWM+C spatial resolution was too coarse to resolve wave

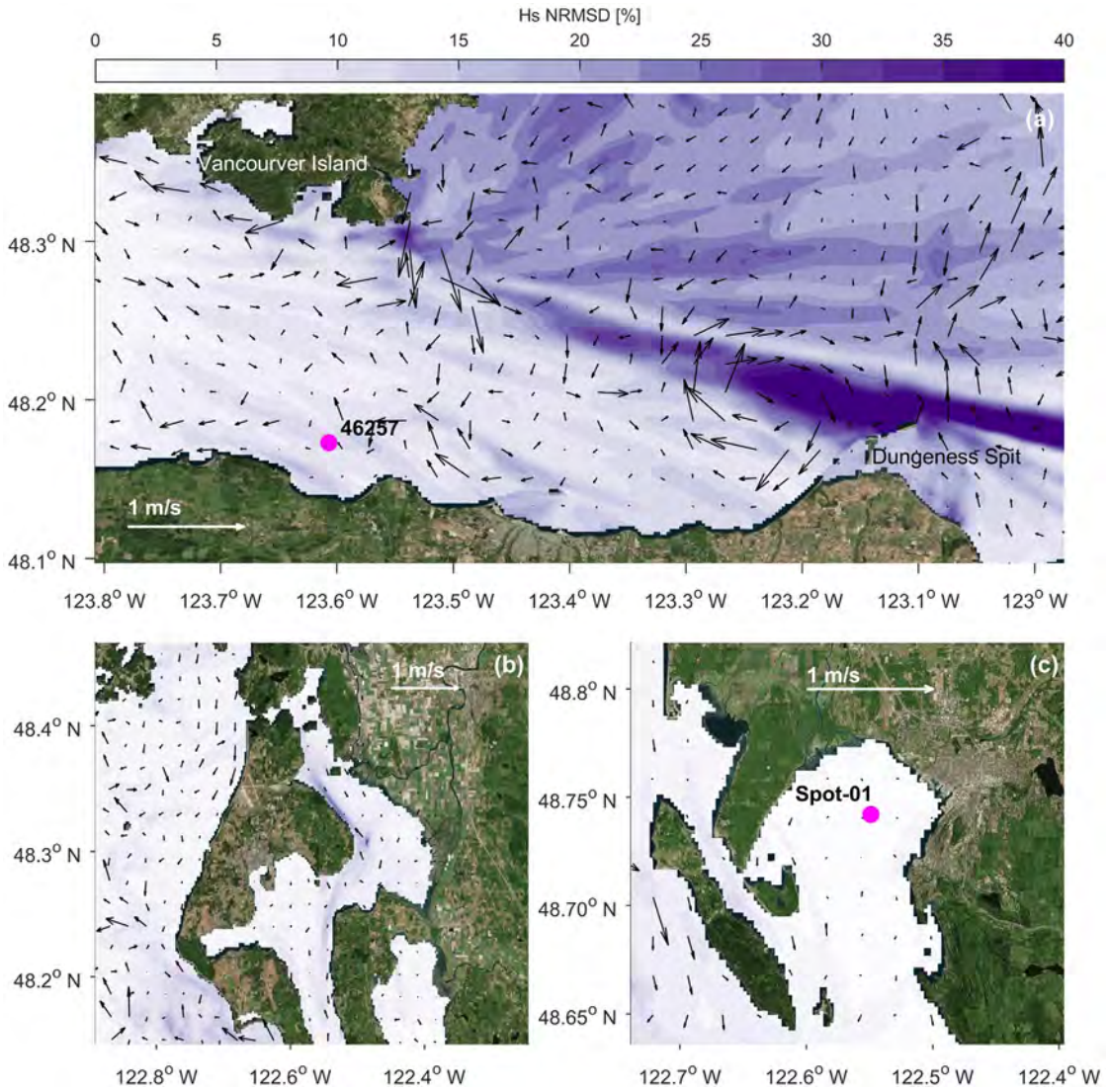

Fig. 7. Normalized root-mean-squared-difference (NRMSD, see appendix A.1) between stationary with currents (SWM+C) and without (SWM) predictions for domains (a) D2, (b) D3, and (c) D4 (Table 2) for predictions from October to November 2020. Black arrows show mean depth-averaged current velocity with white arrow and text providing scale. Magenta circles show locations wave buoys (Table 1).

generation (Table 2). It is likely the higher resolution LUT predictions more correctly represent wave conditions in these locations.

In the lee of Vancouver Island (eastward), just inside the SJF, LSR+LUT predicted wave height are slightly smaller (10%–30%) than SWM+C, appearing to diffuse less northward energy into basin. The north–south gradient caused by the sheltering by Vancouver island is sharper for LSR+LUT than for SWM+C. While diffraction is not used in any models, non-linear wave–wave interactions not captured in LSR+LUT may increase directional spreading breaking down sharp sheltering gradients. Additionally, model spatial and directional resolutions vary significantly and model numerics may also be responsible for reducing gradients in comparatively coarser resolutions.

4.5. Trade-offs

Non-stationary SWAN simulations, at the spatial resolution needed to resolve details of a domain such as the Salish Sea, are currently impractical for long-term simulations. While the use of unstructured grids has allowed for some progress (Yang et al., 2019) it is unclear whether sheltering details in the SJF are properly resolved or if such a method is practical for much longer simulations. The relatively short (2-month) non-stationary simulations presented here required 9 days to complete on a 2 Intel® Xeon® Processor E3-1276 v3 nodes (4-cores each), a computational cost approximately 3x that of comparable stationary simulations. This 3x increase in required expense reduced wave height errors by a relatively modest 1–2 cm at 46257 and Spot-1 observation sites (Table 4) and exhibited relatively small root-mean-squared-differences of 0–10 cm between models across the domain (Fig. 5c).

While comparatively faster, 5-year stationary simulations (SWM+C) required 14 days to complete on 12 nodes (4-cores each), for many, this represents an insignificant computational cost. In addition, traditional SWAN implementations must be run again to revise predictions if input forcing is updated or modified. This is not uncommon in climate change scenario downscaling where new global forcings become available with each iteration of model development. Typically these simulations are long (100+ years), and have multiple scenarios, *e.g.,* representative

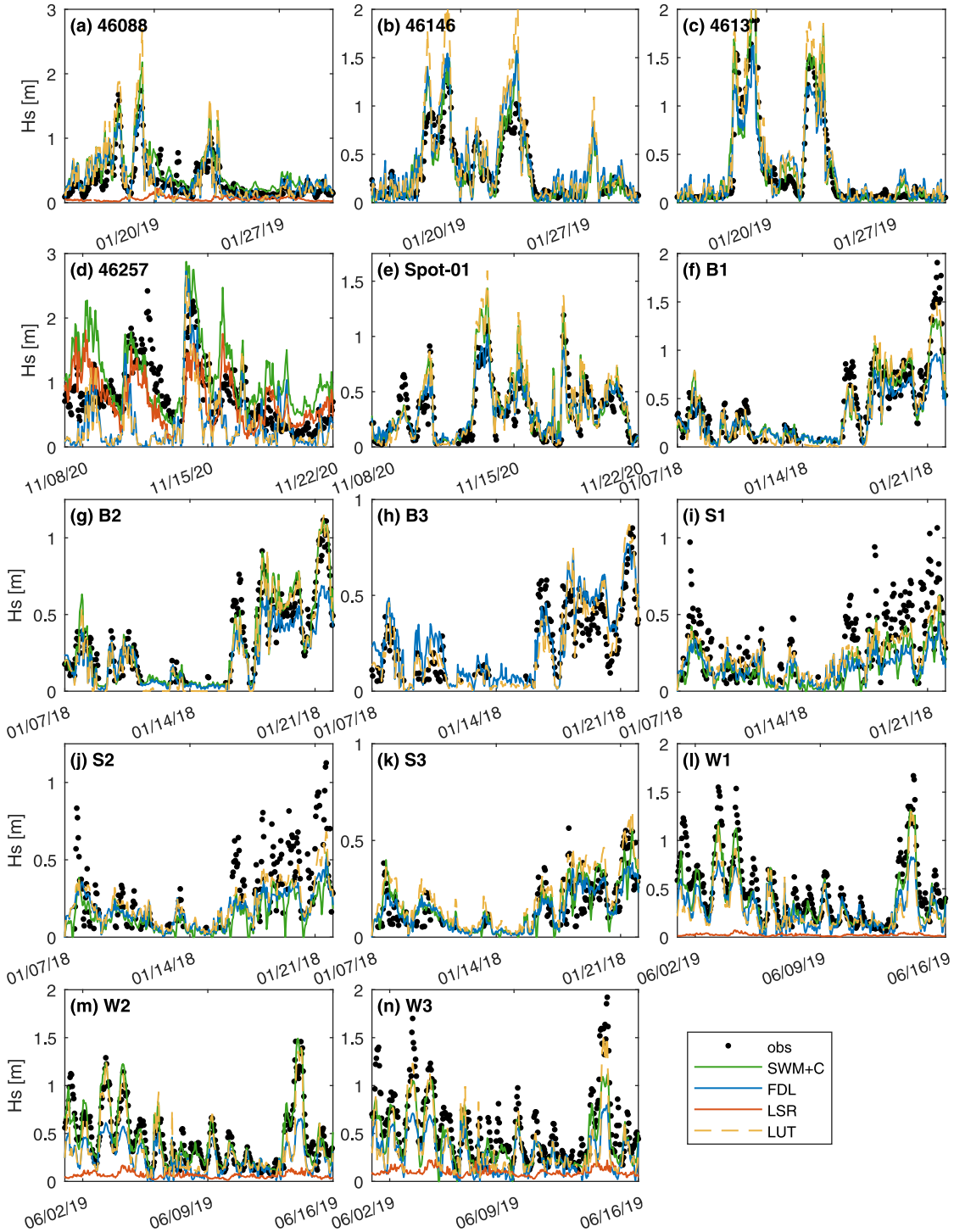

Fig. 8. Model-predicted (colors) and observed (black dots) wave heights versus time at varying buoy locations (a–n) for varying model configurations (see legend). Note, LSR predictions are only made at sites exposed to offshore waves, and SWM+C predictions not available at B3 due to its close proximity to land.

concentration pathways (RCPs). A significant advantage of the rapid approaches presented here (FDL, LSR, and LUT) is the insignificant computational cost of producing updated predictions after required simulations are completed.

Though not insignificant, the construction of the LUT suite of simulations (1,728 in total) required approximately 30 days to complete on one Intel Ivy Bridge node (20-cores), about 1/2 of the compute time required by the 5-year stationary model (SWM+C). Albeit, computational expense is not directly comparable between the two due

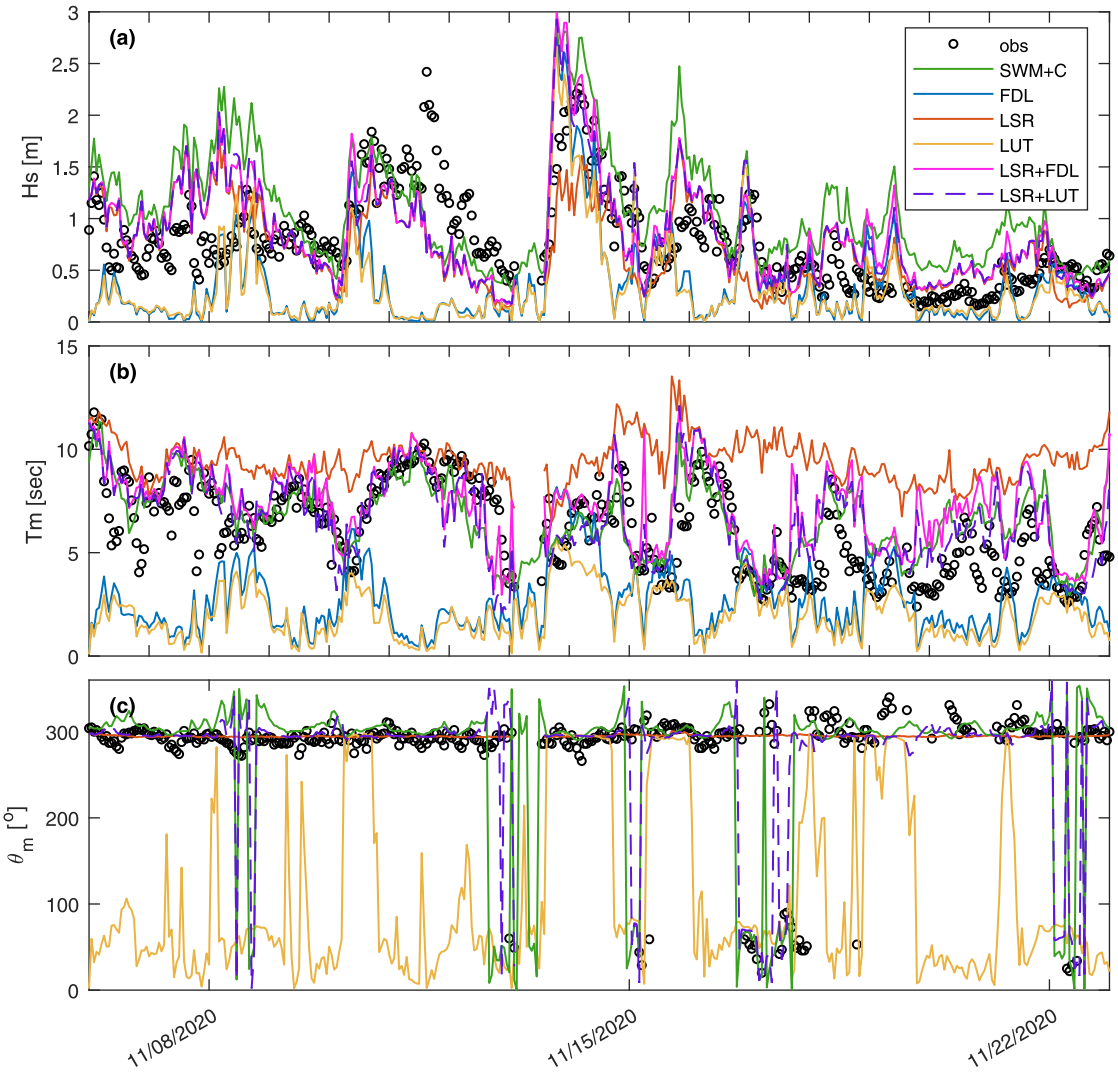

Fig. 9. Model-predicted (colors) and observed (black dots) wave heights (a), mean periods (b), and mean direction (c) versus time at buoy 46257 for varying model configurations (see legend). Note FDL and FDL+LUT mean direction are not shown because the FDL approach does not include a directional component.

to difference in IT-infrastructure. SWAN simulations required by LSR transformation estimates was comparatively trivial, running overnight on a 12-core desktop machine. FDL predictions required the most trivial computational cost as no numerical simulations were needed. For all of these methods, the initial computation was needed only once. Once simulations were completed, predictions were rapidly made for any set of forcing conditions (5-year interpolations can be completed in minutes).

At observation sites considered here, RMSE of LSR+LUT and LSR +FDL methods were within 4 cm and 0.5 s of SWM+C errors for wave height and mean period, respectively. Normalized bias and RMSD between these reduced-physics models and SWM+C range from 0%–30% in most of the regions. In terms of absolute error to observations, the relative gain in accuracy with a traditional SWAN implementation was found to be considerably small. Differences between models varied over the region. In modestly sized bays with minimal exposure to remotely generated waves differences were quite small. While larger differences were observed in more dynamic regions such as the SJF (Fig. 7), without additional observations, conclusions about absolute errors and improvement cannot made.

In addition to computational savings, LSR and LUT approaches allow for higher spatial resolution than what is practical in traditional SWAN implementations. While resolution varied from 50–1,000 meters in nested SWM+C domains, LSR and LUT predictions were made on 50-m and 100-m resolution grids across the Puget Sound (L2) and larger Salish Sea region (L1, LSR, Table 2) with the potential to resolve nearshore wave conditions more accurately.

Overall these rapid approaches reduce computation cost by 2–4 orders of magnitude while incurring a relatively small loss in accuracy (Table 5), that may be larger in highly dynamic regions. Implementation is relatively straightforward, but more complex than traditional model building. Such rapid frameworks excel most strongly where high resolution and very long predictions are required.

5. Summary

In the Salish Sea region stationary SWAN assumptions result in only minor skill degradation (Table 4). SWAN simulations show that while including currents effects had negligible impact to skill at observation sites available (Table 4), spatial wave are likely significantly effected in the SJF near Dungeness Spit (Fig. 6).

Overall, rapid implementations of fetch-limited, look-up-table, and linear spectral refraction are skill-full in much of the region as com-

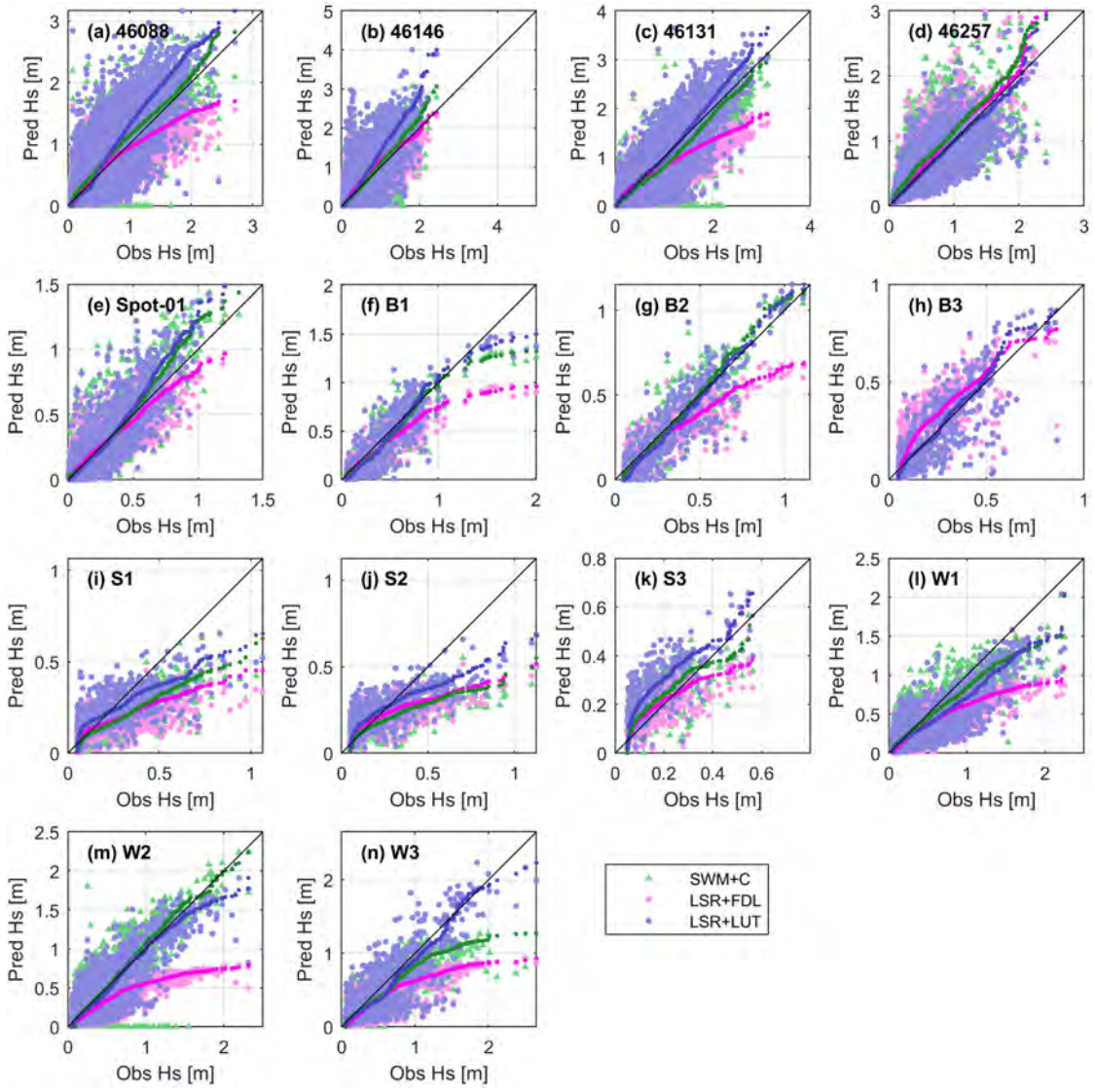

Fig. 10. Quantile–quantile (q–q) plots of observed (x-axis) and model-predicted (y-axis) wave height. Different colors represent different model configurations with lighter colors depicting observations and darker colors their quantiles. In particular, stationary swan with current (SWM+C), LSR+FDL and LSR+LUT are shown.

pared to traditional SWAN simulations (Table 5). Combinations of these methods appear to capture both remotely and locally generated waves well, despite missing non-linear interactions between them. Additionally, model–model comparisons show lower root-mean-squared-differences than compared with observations (Fig. 11) suggesting that prediction error may be due to uncertainties in model boundary forcing, *e.g.,* errors in wind predictions, uncertainties in directional details of offshore waves, and errors in bathymetry.

The rapid approaches presented here may server as a framework for rapid coastal prediction where local, remote, or both types of wave energy are prevalent. The methods require orders of magnitude (2–4) less computation than traditional SWAN implementations and are well suited to support both rapid near-term forecast systems and long-term, high-resolution, historical or future simulations needed to evaluate robust wave statistics alongshore.

CRediT authorship contribution statement

Sean C. Crosby: Model framework development, Implementation, Analysis, Study design. **Cornelis M. Nederhoff:** Coupled model development and implementation. **Nathan VanArendonk:** High performance computer model simulations. **Eric E. Grossman:** Wrote funding proposal, Lead larger effort.

Declaration of competing interest

The authors declare that they have no known competing financial interests or personal relationships that could have appeared to influence the work reported in this paper.

Data availability

Data will be made available on request

Acknowledgments

Funding for this project included a grant from the U.S. Environmental Protection Agency (DW-014-92478501-0) to Dr. Eric Grossman of the U.S. Geological Survey Pacific Coastal and Marine Science Center and support of the USGS Coastal and Marine Hazards and Resources Program. We also thank Washington Department of Natural Resources and the Swinomish Indian Tribal Community for collaborations conducting oceanographic deployments on their tidal lands.

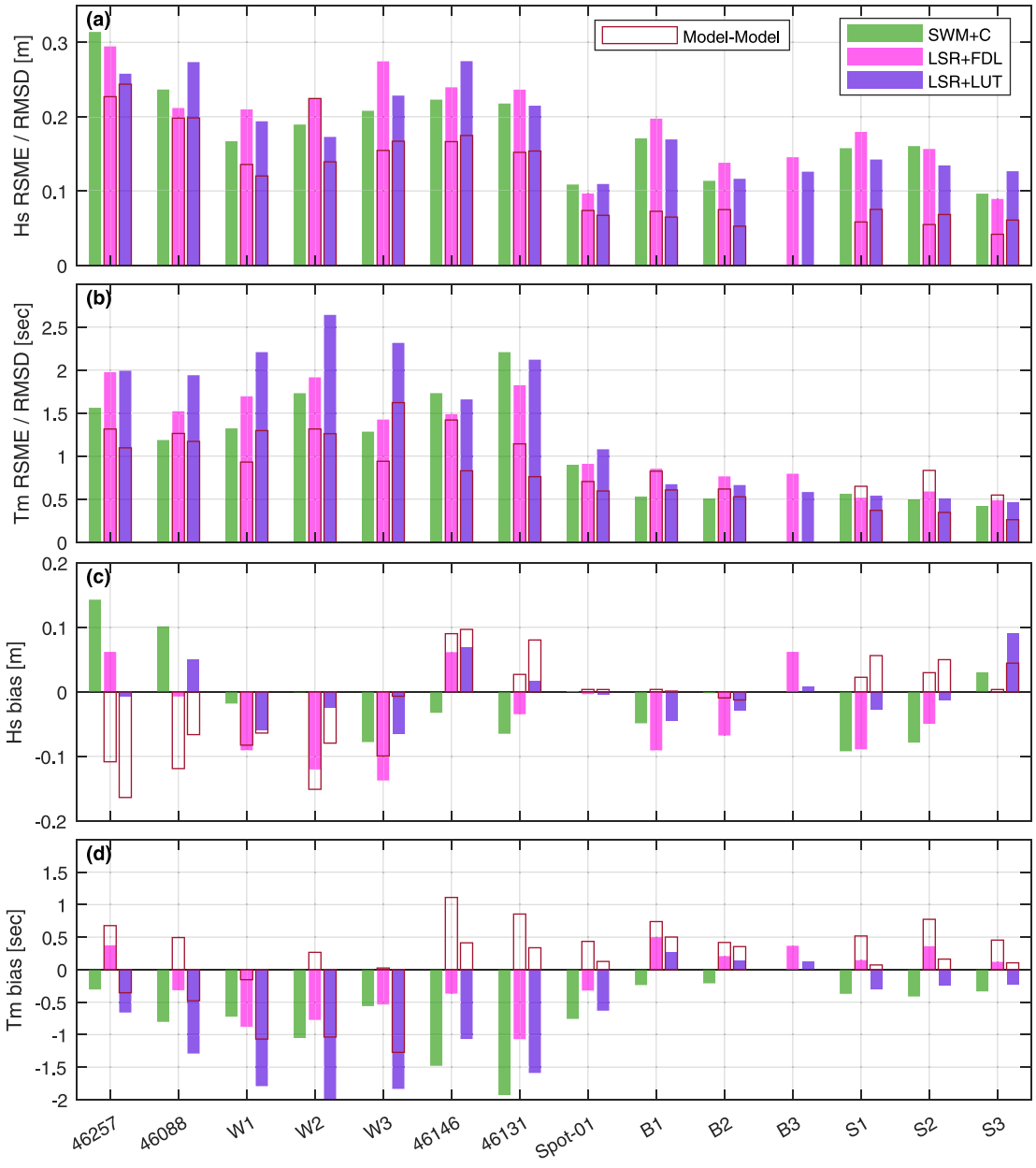

Fig. 11. Root-mean-square-error (RMSE) and bias of predicted wave heights (a,c) and mean periods (b,d) versus observation location for varying model configurations (see legend). Dark red outlines show root-mean-squared-difference (RMSD) and bias between the outlined model and SWAN+C, illustrating relative magnitude of model–model error to model-observation error.

Appendix

A.1. Error metrics

The error metrics used throughout are defined here. Mean bias is defined as,

$$\text{bias} = \frac{1}{T}\sum_{i=1}^{T}(p_i - o_i)\,, \tag{10}$$

where predictions, p, and observations, o, are taken from each valid time step, i. Similarly, Root-Mean-Square-Error (RMSE) is estimated by,

$$\text{RMSE} = \sqrt{\frac{1}{T}\sum_{i=1}^{T}(p_i - o_i)^2}\,. \tag{11}$$

Normalized metrics are estimated by dividing by mean values after computation rather than determining mean errors from normalized values at each time-step. These definitions weight larger values more heavily, ignoring large relative errors during periods of low energy. Here, normalized-bias (Nbias) is defined as,

$$\text{Nbias} = 100 \cdot \frac{\frac{1}{T}\sum_{i=1}^{T}(p_i - o_i)}{\frac{1}{T}\sum_{i=1}^{T} o_i}\,, \tag{12}$$

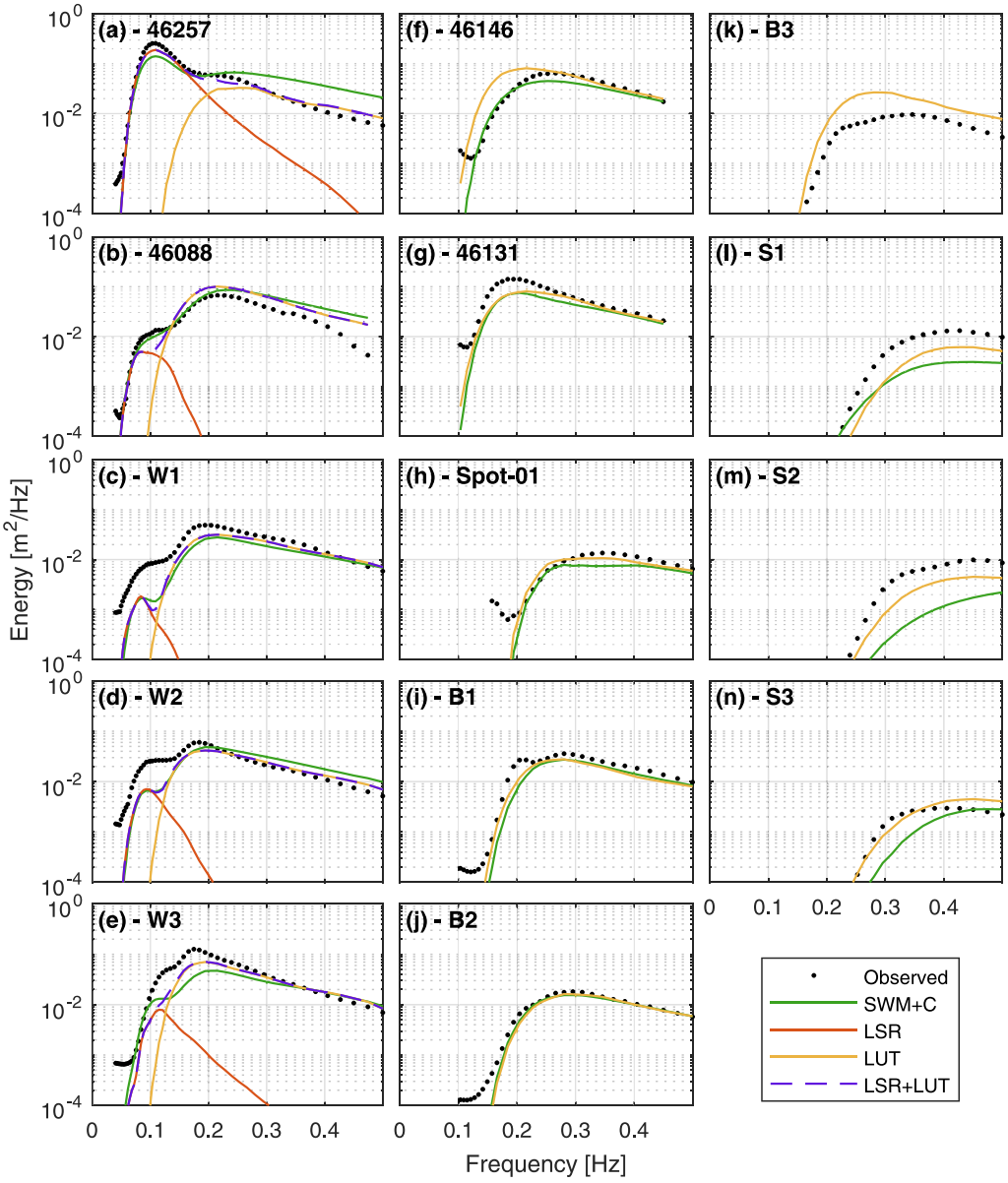

Fig. 12. Mean modeled (colored lines) and observed (black dots) energy versus frequency at observations sites exposed to offshore wave energy in panels (a)–(e). Modeled and observed energy averaged over time frames where observations are available (Table 1).

and normalized-root-mean-squared-error (NRMSE) is defined as

$$\mathrm{NRMSE} = 100 \cdot \frac{\sqrt{\frac{1}{T}\sum_{i=1}^{T}(p_i - o_i)^2}}{\frac{1}{T}\sum_{i=1}^{T} o_i}. \tag{13}$$

Here, errors are considered as the difference between model and observations. Additionally we consider the difference between models, such as the bias and normalized-root-mean-squared-difference (RMSD). These consider same formula above, but swap o with some reference model prediction, *e.g.*, p_{ref}. Here the reference model is typically the more complex model, where the goal is to determine what is missing, error-wise, in the simplified model.

A.2. Fetch-depth-limited optimization

FDL predictions can be made rapidly, and with two free parameters, α and β, may be optimized. Here, LSR predictions are added (LSR+FDL) for locations exposed to remotely generated energy. Wave height RMSE vary for LSR+FDL predictions over a range of α and β values (Fig. A1). Optimal α and β values minimize wave height RMSE and are indicated by red circles in Fig. A1 at varying observation location. Optimal values were not consistent between observation locations (Table 1). Despite occupying similar large basins without offshore wave exposure, lowest RMSEs at 46146 were observed with small β values while 46131 indicated a larger β yielded better skill (Fig. A1b,c). Observations in

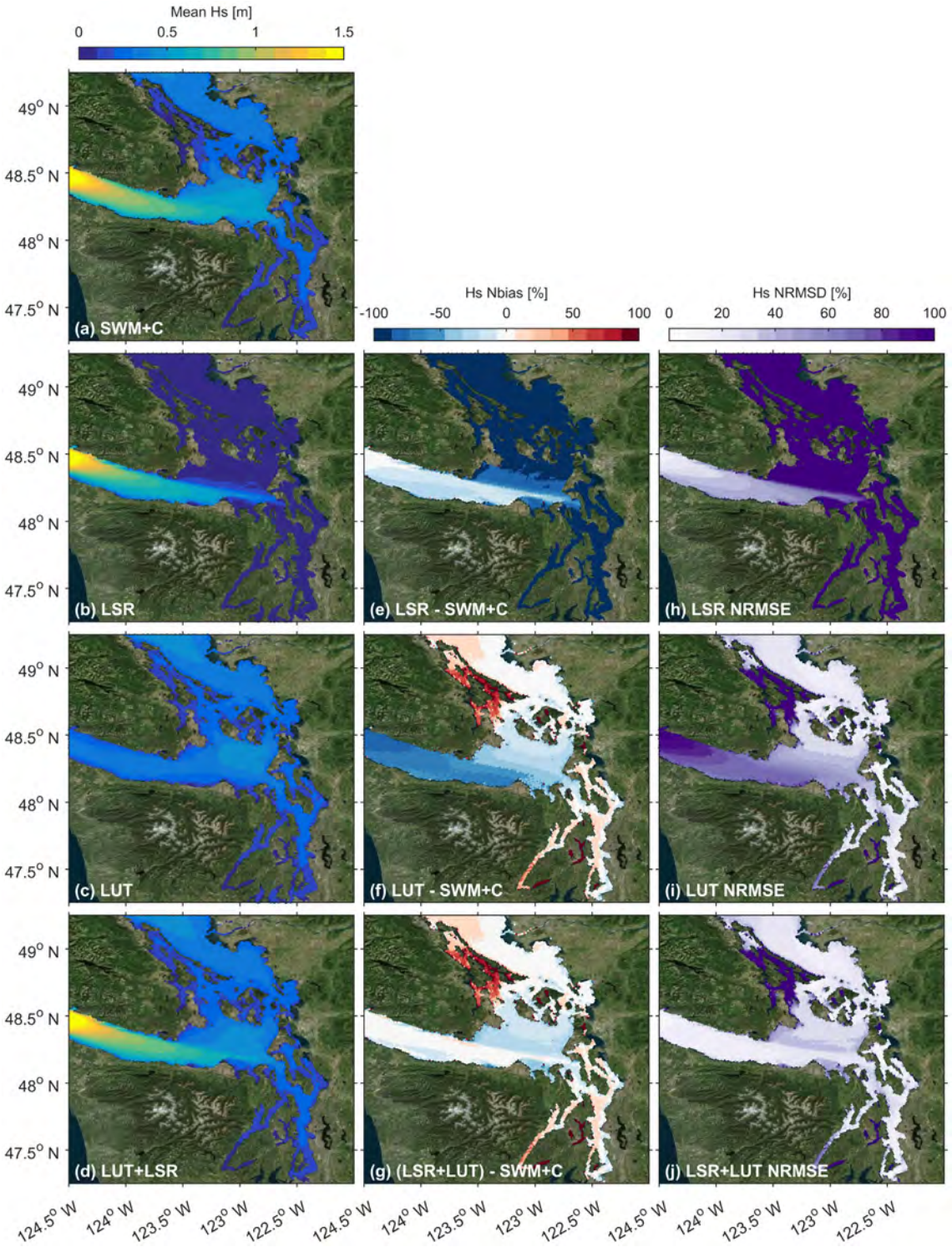

Fig. 13. Mean SWM (a), LSR (b), LUT (c), and LSR+LUT (d) modeled wave heights from Oct 1 2020 through Nov 30 2020. Mean bias with SWM+C predictions for LSR (e), LUT (f), and LSR+LUT (g). Root-mean-squared-difference (RMSD) with SWM+C predictions for LSR (h), LUT (i), and LSR+LUT (j).

Bellingham Bay (B1–B3) show similar disagreement for preferred α and β values.

The observed lack of agreement of optimal α and β values, even in similar locations, suggest that these parameters are compensating for wind forcing uncertainties or limitations of the empirical method itself. Additionally, while here wind input is taken at the nearest over-water prediction location to the prediction location, a more sophisticated approach would be take a weighted average of up-wind wind conditions, and an optimization of plausible weight parameters may yield more consistent results. Nonetheless, for simplicity, here errors were

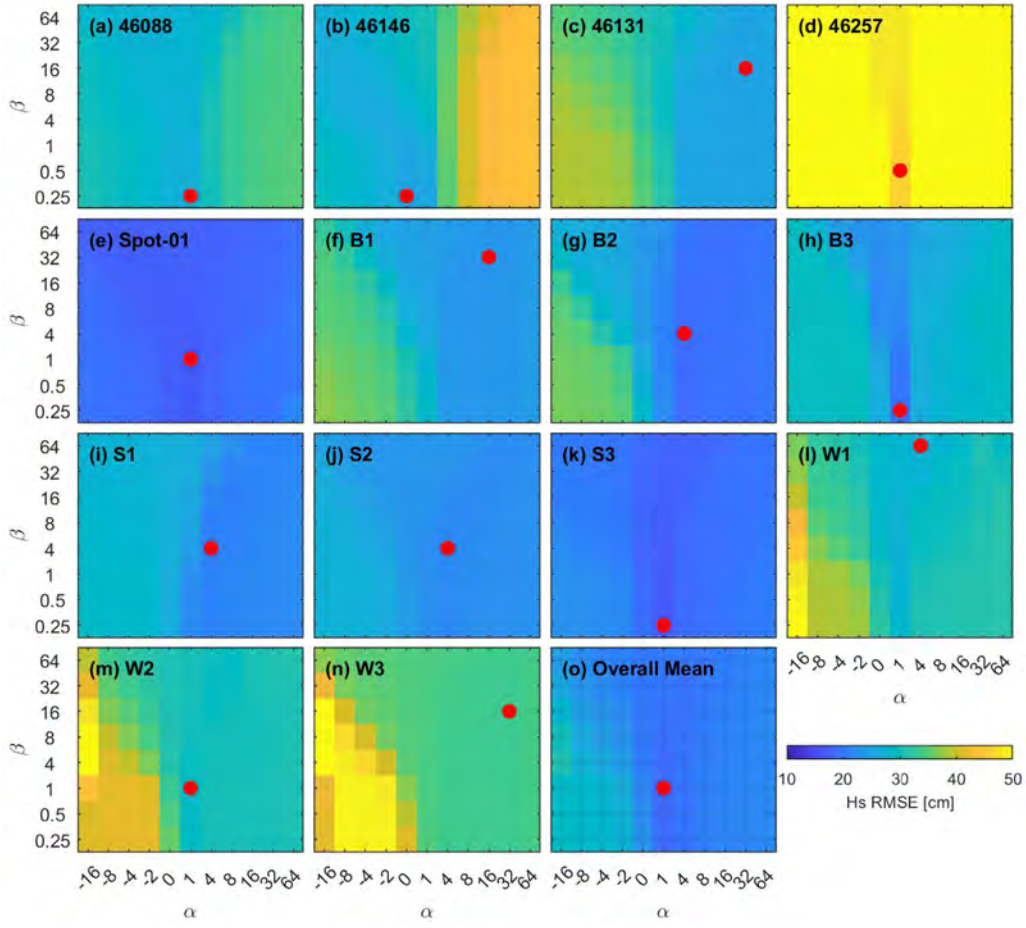

Fig. A1. H_s root-mean-squared-error (RMSE) versus α and β at each observation site (Table 1) and a simple average across all locations except for 46257 due to its high exposure to remotely generated waves (n). Minimum RMSE is indicated by the filled red circle.

averaged across all sites and an optimal average value of $\beta = 1$ and $\alpha = 1$ (Fig. A1o) was therefore used in the following analysis across the region.

References

Anon, 2021. USGS Advanced research computing, USGS Yeti supercomputer: U.S. geological survey. http://dx.doi.org/10.5066/F7D798MJ.

Ardhuin, F., Gille, S.T., Menemenlis, D., Rocha, C.B., Rascle, N., Chapron, B., Gula, J., Molemaker, J., 2017. Small-scale open ocean currents have large effects on wind wave heights. J. Geophys. Res.: Oceans 122, 4500–4517.

Battalio, B., Chandrasekera, C., Divoky, D., Hatheway, P.D., Hull, C.T., Bill, P.O., Seymour, D., Srinivas, P.R., Hatheway, D.D.D., 2005. Wave Transformation: FEMA Coastal Flood Hazard Analysis and Mapping. Federal Emergency Management Agency FEMA, Washinton DC.

Booij, N., Ris, R.C., Holthuijsen, L.H., 1999. A third-generation wave model for coastal regions: 1. Model description and validation. J. Geophys. Res. 104, 7649–7666.

Camus, P., Mendez, F.J., Medina, R., 2011. A hybrid efficient method to downscale wave climate to coastal areas. Coast. Eng. 58, 851–862.

Camus, P., Mendez, F.J., Medina, R., Tomas, A., Izaguirre, C., 2013. High resolution downscaled ocean waves (DOW) reanalysis in coastal areas. Coast. Eng. 72, 56–68.

Canada, E., 2019. Historic hydrometric data extracted from the environment and climate change Canada historical hydrometric data web site. Date Accessed: Dec 2020.

CERC, 1984. Shore Protection Manual Book II. U.S. Army Coastal Engineering Research Center, Corps of Engineers, Vicksburg, Mississippi.

Crosby, S.C., Grossman, E.E., 2019. Wave observations from nearshore bottom-mounted pressure sensors in Skagit and Bellingham Bays, Washington, USA from Dec 2017 to Feb 2018. U. S. Geological Survey.

Crosby, S.C., Kumar, N., O'Reilly, W.C., Guza, R.T., 2018. Regional swell transformation by backward ray tracing and SWAN. J. Atmos. Ocean. Technol. 36, 217–229.

Crosby, S.C., O'Reilly, W.C., Guza, R.T., Crosby, S.C., O'Reilly, W.C., Guza, R.T., 2016. Modeling long-period swell in southern California: Practical boundary conditions from Buoy observations and global wave model predictions. J. Atmos. Ocean. Technol. 33, 1673–1690.

Dorrestein, R., 1960. Simplified method of determining refraction coefficients for sea waves. J. Geophys. Res. 65, 637–642.

Elliott, A.J., Neill, S.P., 2015. Simulating storm waves in the Irish sea, vol. 160. pp. 57–64, http://dx.doi.org/10.1680/Maen.2007.160.2.57.

Erikson, L.H., Hegermiller, C.A., Barnard, P.L., Ruggiero, P., van Ormondt, M., 2015. Projected wave conditions in the eastern north Pacific under the influence of two CMIP5 climate scenarios. Ocean Model. 96, 171–185.

Finlayson, D., 2006a. The Geomorphology of Puget Sound Beaches. Puget Sound Nearshore Partnership / University of Washington, Seattle.

Finlayson, D.P., 2006b. The Geomorphology of the Puget Sound Beaches. University of Washington, Tides are mixed semidurnal, near 180-deg phase relationship between diurnal and semidurnal results in two nearly equal high tides and extreme low tide, this leads to water level assymetry in tidal levels.
NTR=obs - pred. Wrong. This leads to incorrect estimates of NTR extreme probabilities per month. Additionaly yearly averages of slp and tide level lead to 19.4 mm/mb. I could not replicate this. My estimates are much lower with properly filtered observations.

Gallet, B., Young, W.R., 2014. Refraction of swell by surface currents. J. Mar. Res. 72, 105–126.

García-Medina, G., Özkan-Haller, H.T., Ruggiero, P., Oskamp, J., 2013. An inner-shelf wave forecasting system for the U.S. Pacific northwest. Weather Forecast. 28, 681–703.

Gerstel, W.J., Brunengo, M.J., Lingley, Jr., W.S., Logan, R.L., Shipman, H., Walsh, T.L., 1997. Puget sound bluffs: The where, why, and when of landslides following the holiday 1996/97 storms. Washington Geol. 25.

Golshani, A.A., 2011. A 60 Years wave hindcast study in the south of Persian GULF Using swan model & semi-time domain method. J. Mar. Eng, 6, 73–87.

Hasselmann, K., Barnett, T.P., Bouws, E., Carlson, H., Cartwright, D.E., Enke, K., Ewing, J.A., Gienapp, H., Hasselmann, D.E., Kruseman, P., Meerburg, A., Muller, P., Olbers, D.J., Richter, K., Sell, W., Walden, H., 1973. Measurements of wind-wave growth and swell decay during the joint north sea wave project (JONSWAP). Ergnzungsheft Zur Deutschen Hydrographischen Zeitschrift Reihe A(8), p.95.

Hegermiller, C.A., Rueda, A., Erikson, L.H., Barnard, P.L., Antolinez, J.A.A., Mendez, F.J., 2017. Controls of multimodal wave conditions in a Complex Coastal setting. Geophys. Res. Lett. 44, 12,315–12,323.

Hegermiller, C.A., Warner, J.C., Olabarrieta, M., Sherwood, C.R., 2019. Wave–current interaction between hurricane Matthew wave fields and the gulf stream. J. Phys. Oceanogr. 49 (11), 2883–2900.

Jones, N.L., Monismith, S.G., 2007. Measuring short-period wind waves in a tidally forced environment with a subsurface pressure gauge. Limnol. Oceanogr.: Methods 5, 317–327.

Kernkamp, H.W., Van Dam, A., Stelling, G.S., De Goede, E.D., 2011. Efficient scheme for the shallow water equations on unstructured grids with application to the Continental Shelf. Ocean Dyn. 61 (8), 1175–1188.

Kumar, N., Cahl, D.L., Crosby, S.C., Voulgaris, G., 2017. Bulk versus spectral wave parameters: Implications on Stokes drift estimates, regional wave modeling, and HF radars applications. J. Phys. Oceanogr. 47, 1413–1431.

Lambrakos, K.F., 1981. Wave-current interaction effects on water velocity and surface wave spectra. J. Geophys. Res. 86, 10955.

Leijnse, T., van Ormondt, M., Nederhoff, K., van Dongeren, A., 2021. Modeling compound flooding in coastal systems using a computationally efficient reduced-physics solver: Including fluvial, pluvial, tidal, wind- and wave-driven processes. Coast. Eng. 163, 103796.

Longuet-Higgins, M.S., 1957. On the transformation of a continuous spectrum by refraction. Math. Proc. Camb. Phil. Soc. 53, 226.

Longuet-Higgins, M., Cartwright, D., Smith, N., 1963. Observations of the directional spectrum of sea waves using the motions of a floating buoy. In: Proceedings of the Royal Society of London. Series a, Mathematical and Physical Sciences. Easton, Maryland, pp. 111–136.

Lyard, F., Carrere, L., Cancet, M., Guillot, A., Picot, N., 2017. FES2014, a new finite elements tidal model for global ocean. Ocean Dynam. 10.

Lygre, A., Krogstad, H.E., 1986. Maximum entropy estimation of the directional distribution in ocean wave spectra. J. Phys. Oceanogr. 16, 2052–2060.

Mehaute, L.B., Wang, J.D., Mehaute, B.L., Wang, J.D., 1982. Wave spectrum changes on sloped beach. J. Waterw. Port Coast. Ocean Div. 108, 33–47.

Munk, W.H., O'Reilly, W.C., Reid, J.L., 1988. Australia-Bermuda sound transmission experiment (1960) revisited. J. Phys. Oceanogr. 18, 1876–1898.

Ochoa, J., Delgado-González, O.E., 1990. Pitfalls in the estimation of wind wave directional spectra by variational principles. Appl. Ocean Res. 12, 180–187.

O'Reilly, W.C., Guza, R.T., 1991. Comparison of spectral refraction and refraction-diffraction wave models. J. Waterw. Port Coast. Ocean Eng. 117, 199–215.

O'Reilly, W., Guza, R., 1993. A comparison of two spectral wave models in the southern California bight. Coast. Eng. 19, 263–282.

O'Reilly, W.C., Herbers, T.H.C., Seymour, R.J., Guza, R.T., 1996. A comparison of directional Buoy and fixed platform measurements of Pacific swell. J. Atmos. Ocean. Technol. 13, 231–238.

O'Reilly, W., Olfe, C.B., Thomas, J., Seymour, R., Guza, R., 2016. The California coastal wave monitoring and prediction system. Coast. Eng. 116, 118–132.

Survey, U.G., 2016. National water information system data available on the world wide web (USGS water data for the nation). Date Accessed: Dec 2020.

Sweet, W., Hamlington, B., Kopp, R., Weaver, C., Barnard, P., Bekaert, D., Brooks, W., Craghan, M., Dusek, G., Frederikse, T., Garner, G., Genz, A., Krasting, J., Larour, E., Marcy, D., Marra, J., Obeysekera, J., Osler, M., Pendleton, M., Roman, D., Schmied, L., Veatch, W., White, K., Zuzak, C., 2022. Global and Regional Sea Level Rise Scenarios for the United States. Technical Report NOS 01. National Oceanic and Atmospheric Administration, National Ocean Service, Silver Spring, MD, National Oceanic and Atmospheric Administration, National Ocean Service, Silver Springs, MD, p. 111.

Tehranirad, B., Crosby, S., Stevens, A.W., Grossman, E.E., VanArendonk, N., Nowacki, D., Nederhoff, K., Erikson, L., Barnard, P., 2023. Extreme water levels in the Salish sea: A new method to simulate sea level anomalies. Ocean Model. Rev..

Thompson, R.E., Thomson, R.E., 1994. Physical oceanography of the strait of Georgia-Puget Sound-Juan de Fuca strait system. In: Symposium on the Marine Environment, Vol. 1948. Sydney, B.C., pp. 36–100.

Tyler, D., Danielson, J., Grossman, E., Hockenberry, R., 2020. Topobathymetric model of puget sound, washington, 1887 to 2017. Science Base.

Tyler, D., Danielson, J., Grossman, E., R.J., .H., 2021. Topobathymetric model of the strait of Juan de Fuca, 1891 to 2016. Sci. Base.

Yang, Z., García-Medina, G., Wu, W.C., Wang, T., Leung, L.R., Castrucci, L., Mauger, G., 2019. Modeling analysis of the swell and wind-sea climate in the Salish sea. Estuar. Coast. Shelf Sci. 224, 289–300.

Young, I., Verhagen, L., 1996. The growth of fetch limited waves in water of finite depth. Part 1. total energy and peak frequency. Coast. Eng. 29, 47–78.